SUPPORTING INFORMATION

Fast photoswitchable molecular prosthetics control neuronal activity in the cochlea

Aida Garrido-Charles[1,2,3,4,5~], Antoine Huet[3,4,5,6~], Carlo Matera[1,2,7~], Anupriya Thirumalai[3,4,6], Jordi Hernando[8], Amadeu Llebaria[9], Tobias Moser[3,4,5#*], Pau Gorostiza[1,2,10#*]

[1]Institute for Bioengineering of Catalonia (IBEC), Barcelona Institute for Science and Technology, Carrer de Baldiri Reixac 15-21, 08028 Barcelona, Spain

[2]Network Biomedical Research Center in Bioengineering, Biomaterials, and Nanomedicine (CIBER-BBN), 28029 Madrid, Spain

[3]Institute for Auditory Neuroscience and InnerEarLab, University Medical Center Göttingen, 37075 Göttingen, Germany.

[4]Auditory Neuroscience and Optogenetics Group, German Primate Center, 37077 Göttingen, Germany.

[5]Cluster of Excellence "Multiscale Bioimaging: from Molecular Machines to Networks of Excitable Cells" (MBExC), University of Göttingen, 37075, Göttingen, Germany.

[6]Auditory Circuit Lab, Institute for Auditory Neuroscience and InnerEarLab, University Medical Center Göttingen, Germany, 37075, Göttingen, Germany.

[7]Department of Pharmaceutical Sciences, University of Milan, Via Luigi Mangiagalli 25, 20133 Milan, Italy

[8] Departament de Química, Universitat Autònoma de Barcelona (UAB), Cerdanyola del Vallès 08193, Spain.

[9]Institute of Advanced Chemistry of Catalonia, Consejo Superior de Investigaciones Científicas (IQAC-CSIC), 08034 Barcelona, Spain.

[10]Catalan Institution for Research and Advanced Studies (ICREA), 08010 Barcelona, Spain

~A.G-C, A.H. and C.M. contributed equally to this work

#T.M. and P.G. contributed equally to this work

*tmoser@gwdg.de (T.M.), pau@icrea.cat (P.G.)

Table of Contents

4. Synthetic protocol for the preparation of TCP_{fast}

5. Characterization of TCP_{fast}, lysine-adduct, and side-product by LC-MS

6. Characterization of TCP_{fast} in cultured neurons

7. *In vivo* photocontrol of neural activity in gerbil's cochlea

8. Sequence alignment and molecular docking simulations

Ligand binding domain sequence alignments of Kainate and AMPA receptors

Molecular Docking Simulations

9. Supporting references

1. General methods and materials for chemical synthesis and physicochemical characterization

All chemicals and solvents are from commercial suppliers and used without purification. All reactions were performed under inert atmosphere of argon. All analytical data of photoisomerizable compounds are given for the *trans* isomer unless otherwise stated. Reactions were monitored by thin layer chromatography (TLC: EMD/Millipore, silica gel 60 on aluminum support, layer thickness: 200 µm, particle size: 10-12 µm) by visualization under 254 and/or 365 nm lamp. Flash column chromatography: Panreac Silica Gel 60, 40-63 µm RE. NMR equipment and methods: Varian-Mercury 400 MHz & Varian VNMRS 500 MHz. Chemical shifts (δ) are reported in parts per million (ppm) against the reference compound tetramethylsilane using the signal of the residual non-deuterated solvent [Chloroform-*d* δ = 7.26 ppm (1H), δ = 77.16 ppm (13C); Dimethylsulfoxide-d_6 δ = 2.50 ppm (1H), δ = 39.52 ppm (13C); Methanol-d_4 δ = 3.31 ppm (1H), δ = 49.00 ppm (13C)]. HPLC-PDA-MS equipment and methods: Waters Alliance 2695 separation module coupled to a Waters 2996 photodiode detector (PDA) and a Waters ACQUITY QDa detector (single quadrupole; electrospray ionization), with the MassLynx software for data acquisition; SunFire C18 Column (100 Å, 5 µm, 4.6 mm X 150 mm); injection volume: 5 µL; mobile phase: water w/0.1% formic acid (solvent A) and acetonitrile w/0.1% formic acid (solvent B); elution method: flow 1 mL/min, gradient 0.0-1.0 min, 5% B; 1.0−7.0 min, 5−100% B; 7.0−8.0min, 100% B; 8.0−10.0 min, 100−5% B; runtime 10 min. Waters Alliance 2795 separation module coupled to a Waters 2996 photodiode detector (PDA) and a Waters 3100 Mass Detector (single quadrupole; electrospray ionization), with the MassLynx software for data acquisition; XSelect CSH C18 Column (130 Å, 3.5 µm, 4.6 mm X 50 mm); injection volume: 5 µL; mobile phase: water w/0.1% formic acid (solvent A) and acetonitrile w/0.1% formic acid (solvent B); elution method: flow 1.6 mL/min, gradient 0.0−3.5 min, 5−100% B; 3.5−4.5 min, 100% B; 4.5−5.0 min, 100−5% B; runtime 5 min. Spectra have been scanned between 200 and 800 Da with values every 0.1 seconds and peaks are given as mass/charge (*m*/*z*) ratio. Melting points of solid substances were determined on a Büchi melting point M-565 apparatus and are uncorrected. Optical rotations were measured with a Jasco P-2000 polarimeter operating on a sodium D-line (589 nm) at 25 °C, using a 10-cm path-length cell. High resolution mass spectrometry analyses were performed with a LTQ-FT Ultra Mass Spectrometer (Thermo Scientific) with NanoESI positive ionization. Each sample was reconstituted in MeOH and diluted with CH_3CN/H_2O/formic acid (50:50:1) for MS analysis. The sample was introduced by direct infusion (Automated Nanoelectrospray). The NanoMate (Advion BioSciences, Ithaca, NY, USA) aspirated the samples from a 384-well plate (protein Lobind) with disposable, conductive pipette tips, and infused the samples through the nanoESI Chip (which consists of 400 nozzles in a 20x20 array) towards the mass spectrometer. Spray voltage was 1.70 kV, delivery pressure 0.50 psi and *m*/*z* range 50-2000 Da. Data was acquired with Xcalibur software, vs.2.0SR2 (ThermoScientific). Elemental composition from experimental exact mass monoisotopic value was obtained with a dedicated algorithm integrated in Xcalibur software. Data are reported as mass-to-charge ratio (*m*/*z*) of the corresponding positively charged molecular ion. Transient absorption measurements were registered in a ns laser flash-photolysis system (LKII, Applied Photophysics) equipped with a Nd:YAG laser (Brilliant, Quantel) as a pump source, a Xe lamp as a probe source and a photomultiplier tube (Hamamatsu) coupled to a spectrograph as a detector. All the experiments were carried out in PBS at room temperature (T = 22 °C) and using the third harmonic of the Nd:YAG laser for excitation (λexc = 355 nm, 10 mJ/pulse).

2. Synthetic protocols for the preparation of the 'head' module

Compound **1** ('head' module) was prepared via a 5-step synthesis starting from commercially available materials (Scheme S1). Azobenzene **5** was obtained by reduction of its nitro precursor **4** with sodium sulfide nonahydrate. Pyroglutamate derivative **6**, prepared as previously described[1], was coupled to compound **5** using HOBt/EDC activation to give the intermediate **7**, and then converted via mesylation into the corresponding azide derivative **8**. Hydrolysis of the pyroglutamate moiety with concomitant saponification of the ethyl ester provided the advanced intermediate **9**, which was finally converted into the desired compound **1** via removal of the *tert*-butoxycarbonyl protecting group under acidic conditions.

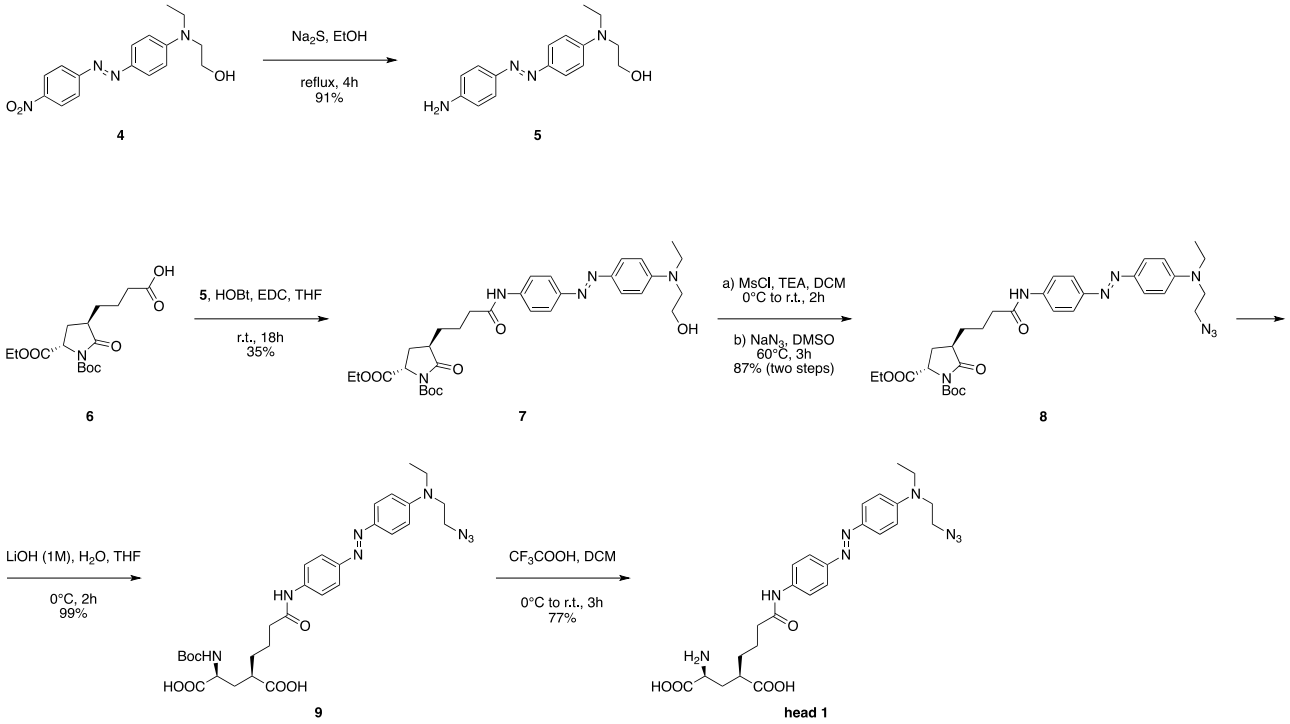

Scheme S1. Chemical synthesis of the 'head' module (compound **1**)

(*E*)-2-((4-((4-aminophenyl)diazenyl)phenyl)(ethyl)amino)ethanol [5]

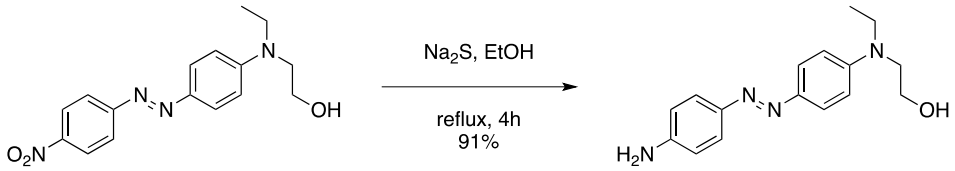

To a solution of (*E*)-2-(ethyl(4-((4-nitrophenyl)diazenyl)phenyl)amino)ethanol [**4**] (2.56 g, 8.14 mmol) in ethanol (250 mL) was added $Na_2S{\cdot}9H_2O$ (2.35 g, 9.77 mmol) and the reaction mixture was refluxed for 4 h. The mixture was then concentrated under reduced pressure and ethyl acetate (200 mL) was added to the residue. The organic layer was washed with water (200 mL) and brine (200 mL), dried over $MgSO_4$, filtered and evaporated under reduced pressure to afford compound [**5**] as a dark red solid which was used in the next step without further purification (2.10 g, 91% yield).

R_f = 0.33 (TLC in cyclohexane/ethyl acetate = 1:1).

m.p. = 144 °C.

^{1}H NMR (400 MHz, CD_3OD) δ 7.73 – 7.66 (m, 2H), 7.64 – 7.58 (m, 2H), 6.83 – 6.77 (m, 2H), 6.77 – 6.71 (m, 2H), 3.74 (t, J = 6.4 Hz, 2H), 3.58 – 3.48 (m, 4H), 1.20 (t, J = 7.1 Hz, 3H).

^{13}C NMR (101 MHz, CD_3OD) δ 151.73, 150.98, 146.24, 144.62, 125.18, 124.95, 115.55, 112.46, 60.35, 53.43, 46.65, 12.45.

HRMS (*m*/*z*) calculated for $C_{16}H_{21}N_4O^+$ $[M+H]^+$: 285.17099, found: 285.17032 (Δ_{ppm} = –2.34).

(2*S*,4*R*)-1-*tert*-butyl 2-ethyl 4-(4-((4-((*E*)-(4-(ethyl(2-hydroxyethyl)amino)phenyl)diazenyl)phenyl) amino)-4-oxobutyl)-5-oxopyrrolidine-1,2-dicarboxylate [7]

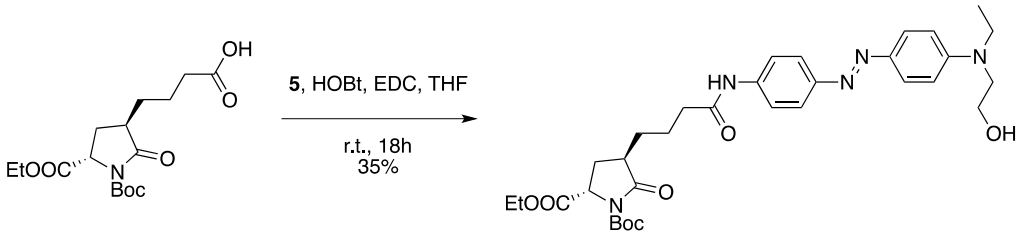

6 **7**

A suspension of 4-((3*R*,5*S*)-1-(*tert*-butoxycarbonyl)-5-(ethoxycarbonyl)-2-oxopyrrolidin-3-yl)butanoic acid [**6**] (250 mg, 0.73 mmol), 1-hydroxybenzotriazole hydrate (HOBt·xH_2O, 223 mg, 1.46 mmol) and *N*-(3-dimethylaminopropyl)-*N*′-ethylcarbodiimide hydrochloride (EDC·HCl, 279 mg, 1.46 mmol) in anhydrous tetrahydrofuran (20 mL) was stirred at room temperature for 30 min. (*E*)-2-((4-((4-aminophenyl)diazenyl)phenyl)(ethyl)amino)ethanol [**5**] (311 mg, 1.09 mmol) was then added and the resulting mixture was stirred at room temperature for 18 h. The solvent was then evaporated and the residue was purified by direct flash chromatography (100% diethyl ether until complete elution of unreacted compound [**5**], then dichloromethane/methanol = 100:0 to 95:5 gradient) to afford compound [**7**] as a dark red oil (156 mg, 35% yield).

R_f = 0.34 (TLC in cyclohexane/ethyl acetate = 2:8).

$[\alpha]_D$ = –3.23 (c = 0.155, methanol).

^{1}H NMR (400 MHz, $CDCl_3$) δ 8.15 (s, 1H), 7.78 (dd, J = 8.9, 6.7 Hz, 4H), 7.64 (d, J = 8.8 Hz, 2H), 6.75 (d, J = 9.2 Hz, 2H), 4.55 (dd, J = 9.6, 1.5 Hz, 1H), 4.22 (q, J = 7.1 Hz, 2H), 3.83 (t, J = 6.0 Hz, 2H), 3.54 (t, J = 6.0 Hz, 2H), 3.48 (q, J = 7.0 Hz, 2H), 2.64 (dtd, J = 11.6, 8.5, 4.7 Hz, 1H), 2.51 (s, 1H), 2.39 (td, J = 7.2, 4.2 Hz, 2H), 2.24 (ddd, J = 13.2, 8.7, 1.5 Hz, 1H), 2.00 (ddd, J = 13.3, 11.7, 9.7 Hz, 1H), 1.94 – 1.82 (m, 1H), 1.76 (ddd, J = 13.7, 10.7, 6.9 Hz, 2H), 1.47 (s, 9H), 1.51 – 1.37 (m, 1H), 1.28 (t, J = 7.1 Hz, 3H), 1.19 (t, J = 7.0 Hz, 3H).

^{13}C NMR (101 MHz, $CDCl_3$) δ 175.75, 171.35, 171.26, 150.45, 149.51, 149.43, 143.67, 139.45, 125.10, 123.12, 120.08, 111.67, 83.87, 61.91, 60.21, 57.38, 52.51, 45.89, 41.64, 37.22, 29.76, 28.45, 28.00, 22.81, 14.32, 12.19.

HRMS (*m*/*z*) calculated for $C_{32}H_{44}N_5O_7^+$ $[M+H]^+$: 610.32353, found: 610.32276 (Δ_{ppm} = –1.25).

(2*S*,4*R*)-1-*tert*-butyl 2-ethyl 4-(4-((4-((*E*)-(4-((2-azidoethyl)(ethyl)amino)phenyl)diazenyl)phenyl) amino)-4-oxobutyl)-5-oxopyrrolidine-1,2-dicarboxylate [8]

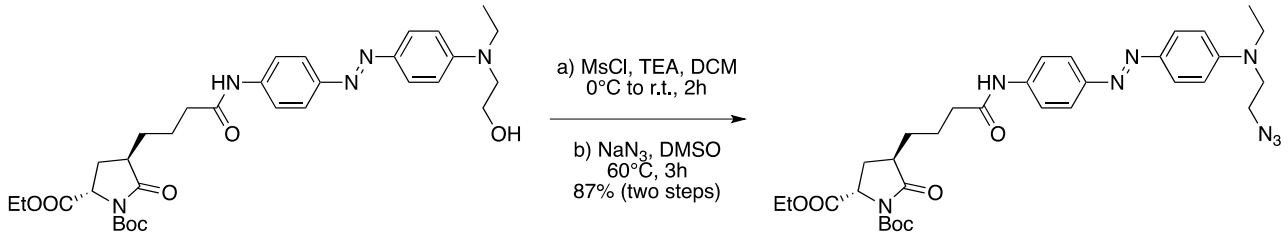

7 **8**

To a solution of (2*S*,4*R*)-1-*tert*-butyl 2-ethyl 4-(4-((4-((*E*)-(4-(ethyl(2-hydroxyethyl)amino) phenyl)diazenyl)phenyl)amino)-4-oxobutyl)-5-oxopyrrolidine-1,2-dicarboxylate [**7**] (136 mg, 0.22 mmol) in anhydrous dichloromethane (15 mL) at 0 °C was added triethylamine (187 μL, 1.34 mmol) followed by a slow addition of methanesulfonyl chloride (86 μL, 1.12 mmol). After 2 h of stirring at room temperature, the filtrate was concentrated to an oil and dissolved in dimethylsulfoxide (2 mL). Sodium azide (73 mg, 1.12 mmol) was then added and the mixture was stirred at 60 °C for 3 h in a sealed vessel. The reaction mixture was then allowed to cool to room temperature, diluted with brine (200 mL) and extracted with diethyl ether (3 × 200 mL). The combined organic layers were dried over $MgSO_4$, filtered and evaporated to dryness. Purification by direct flash chromatography (*n*-hexane/ethyl acetate = 80:20 to 20:80 gradient) afforded compound [**8**] as an orange oil (123 mg, 87% yield).

R_f = 0.58 (TLC in cyclohexane/ethyl acetate = 2:8).

$[\alpha]_D$ = –2.63 (c = 0.165, methanol).

^{1}H NMR (400 MHz, $CDCl_3$) δ 7.94 (s, 1H), 7.83 (dd, J = 9.9, 9.0 Hz, 4H), 7.68 (d, J = 8.8 Hz, 2H), 6.75 (d, J = 9.2 Hz, 2H), 4.57 (dd, J = 9.6, 1.4 Hz, 1H), 4.23 (q, J = 7.1 Hz, 2H), 3.58 (t, J = 6.0 Hz, 2H), 3.55 – 3.47 (m, 4H), 2.67 (dtd, J = 11.7, 8.4, 4.8 Hz, 1H), 2.43 (td, J = 7.2, 5.0 Hz, 2H), 2.27 (ddd, J = 13.3, 8.7, 1.5 Hz, 1H), 2.02 (ddd, J = 13.3, 11.7, 9.6 Hz, 1H), 1.93 (dtd, J = 17.7, 7.4, 4.8 Hz, 1H), 1.87 – 1.74 (m, 2H), 1.58 – 1.44 (m, 1H), 1.49 (s, 9H), 1.29 (t, J = 7.1 Hz, 3H), 1.23 (t, J = 7.1 Hz, 3H).

^{13}C NMR (101 MHz, $CDCl_3$) δ 175.57, 171.36, 171.03, 149.54, 149.49, 149.47, 144.06, 139.54, 125.14, 123.26, 119.98, 111.63, 83.81, 61.90, 57.35, 49.70, 49.10, 45.92, 41.67, 37.31, 29.78, 28.53, 28.03, 22.84, 14.34, 12.42.

HRMS (*m*/*z*) calculated for $C_{32}H_{43}N_8O_6^+$ $[M+H]^+$: 635.33001, found: 635.32940 (Δ_{ppm} = –0.96).

(2*R*,4*S*)-2-(4-((4-((*E*)-(4-((2-azidoethyl)(ethyl)amino)phenyl)diazenyl)phenyl)amino)-4-oxobutyl)-4-((*tert*-butoxycarbonyl)amino)pentanedioic acid [9]

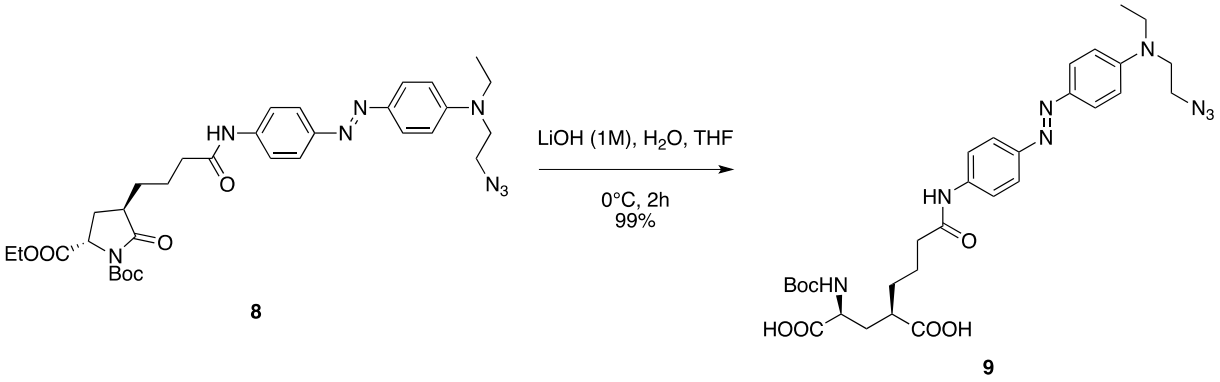

8 **9**

To a solution of (2*S*,4*R*)-1-*tert*-butyl 2-ethyl 4-(4-((4-((*E*)-(4-((2-azidoethyl)(ethyl)amino) phenyl)diazenyl)phenyl)amino)-4-oxobutyl)-5-oxopyrrolidine-1,2-dicarboxylate [**8**] (133 mg, 0.21 mmol) in tetrahydrofuran (6.3 mL) at 0 °C was added a 1.0 M aqueous solution of lithium hydroxide (6.3 mL) and the resulting mixture was stirred at 0 °C for 2 h. The reaction was then acidified to pH 2 with 1.0 M H_2SO_4 and extracted with ethyl acetate (5 × 30 mL). The combined organic layers were dried over $MgSO_4$, filtered and evaporated to dryness to afford compound [**9**] as a dark red oil which was used in the next step without further purification (130 mg, 99% yield).

R_f = 0.55 (TLC in dichloromethane/methanol = 8:2).

$[\alpha]_D$ = +14.57 (c = 0.270, methanol).

^{1}H NMR (400 MHz, CD_3OD) δ 7.81 (d, J = 9.2 Hz, 2H), 7.78 (d, J = 8.9 Hz, 2H), 7.70 (d, J = 9.0 Hz, 2H), 6.87 (d, J = 9.3 Hz, 2H), 4.17 – 4.06 (m, 1H), 3.64 (t, J = 6.1 Hz, 2H), 3.61 – 3.50 (m, 4H), 2.65 – 2.50 (m, 1H), 2.43 (t, J = 7.1 Hz, 2H), 2.30 – 2.12 (m, 1H), 2.10 – 1.89 (m, 1H), 1.88 – 1.67 (m, 4H), 1.67 – 1.55 (m, 1H), 1.44 (s, 9H), 1.24 (t, J = 7.0 Hz, 3H).

^{13}C NMR (101 MHz, CD_3OD) δ 178.71, 176.05, 174.15, 151.36, 150.63, 144.94, 141.34, 125.98, 123.80, 121.22, 112.74, 80.49, 53.56, 50.47, 50.27, 46.49, 43.15, 37.74, 34.90, 33.44, 30.13, 28.73, 24.46, 12.46.

HRMS (*m/z*) calculated for $C_{30}H_{41}N_8O_7^+$ $[M+H]^+$: 625.30927, found: 625.30847 (Δ_{ppm} = –1.28).

(2*S*,4*R*)-2-amino-4-(4-((4-((*E*)-(4-((2-azidoethyl)(ethyl)amino)phenyl)diazenyl)phenyl)amino)-4-oxobutyl)pentanedioic acid [1]

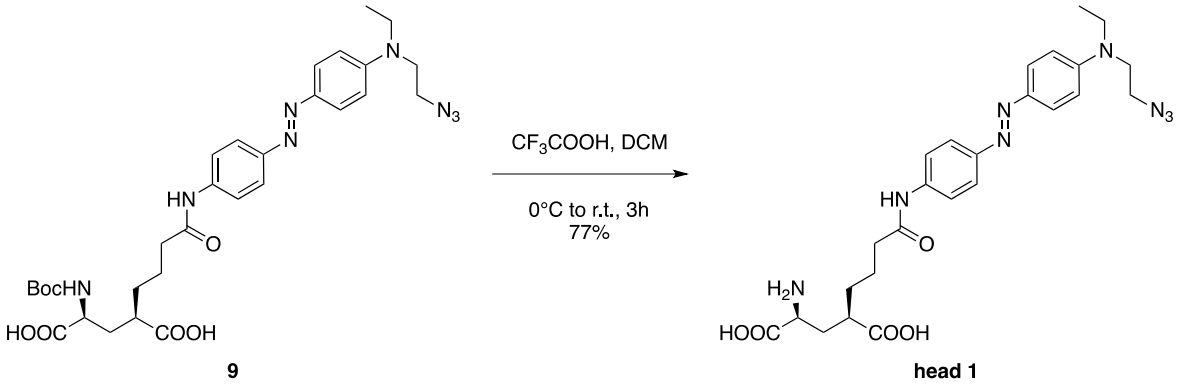

Trifluoroacetic acid (313 μL, 4.09 mmol) was added dropwise to a solution of (2*R*,4*S*)-2-(4-((4-((*E*)-(4-((2-azidoethyl)(ethyl)amino)phenyl)diazenyl)phenyl)amino)-4-oxobutyl)-4-((*tert*-butoxycarbonyl)amino)pentanedioic acid [**9**] (128 mg, 0.20 mmol) in anhydrous DCM (15 mL) at 0 °C, and the resulting solution was stirred at room temperature for 3 h. The solvent was then removed under reduced pressure and the residue was purified by reversed-phase flash chromatography (water/acetonitrile = 100:0 to 0:100 gradient) to afford compound [**1**] as an orange solid (83 mg, 77% yield; purity ≥99% as determined by HPLC-PDA analysis).

R_f = 0.10 (TLC in dichloromethane/methanol = 8:2).

m.p. = 150 °C (dec.).

$[\alpha]_D$ = +11.70 (c = 0.265, methanol).

^{1}H NMR (500 MHz, CD_3OD) δ 7.84 – 7.78 (m, 2H), 7.81 – 7.74 (m, 2H), 7.74 – 7.68 (m, 2H), 6.91 – 6.83 (m, 2H), 3.69 – 3.61 (m, 3H), 3.61 – 3.51 (m, 4H), 2.68 – 2.59 (m, 1H), 2.48 – 2.41 (m, 2H), 2.28 (ddd, J = 14.7, 9.0, 4.7 Hz, 1H), 1.93 (ddd, J = 14.7, 8.5, 4.7 Hz, 1H), 1.86 – 1.72 (m, 4H), 1.72 – 1.61 (m, 2H), 1.24 (t, J = 7.0 Hz, 3H).

^{13}C NMR (126 MHz, CD_3OD) δ 179.72, 174.28, 173.95, 151.35, 150.61, 144.94, 141.39, 125.97, 123.79, 121.21, 112.74, 54.39, 50.48, 50.28, 46.50, 43.51, 37.74, 33.96, 32.71, 24.40, 12.46.

UV-Vis (PBS): λ_{max} (abs) = 460 nm, ε = 2.927 × 10^4 $M^{-1}\cdot cm^{-1}$.

R_t (HPLC-PDA, XSelect CSH C18 Column) = 2.25 min (*trans* isomer).

HRMS (*m*/*z*) calculated for $C_{25}H_{33}N_8O_5^+$ $[M+H]^+$: 525.25684, found: 525.25883 (Δ_{ppm} = +3.78).

3. Supporting Figures

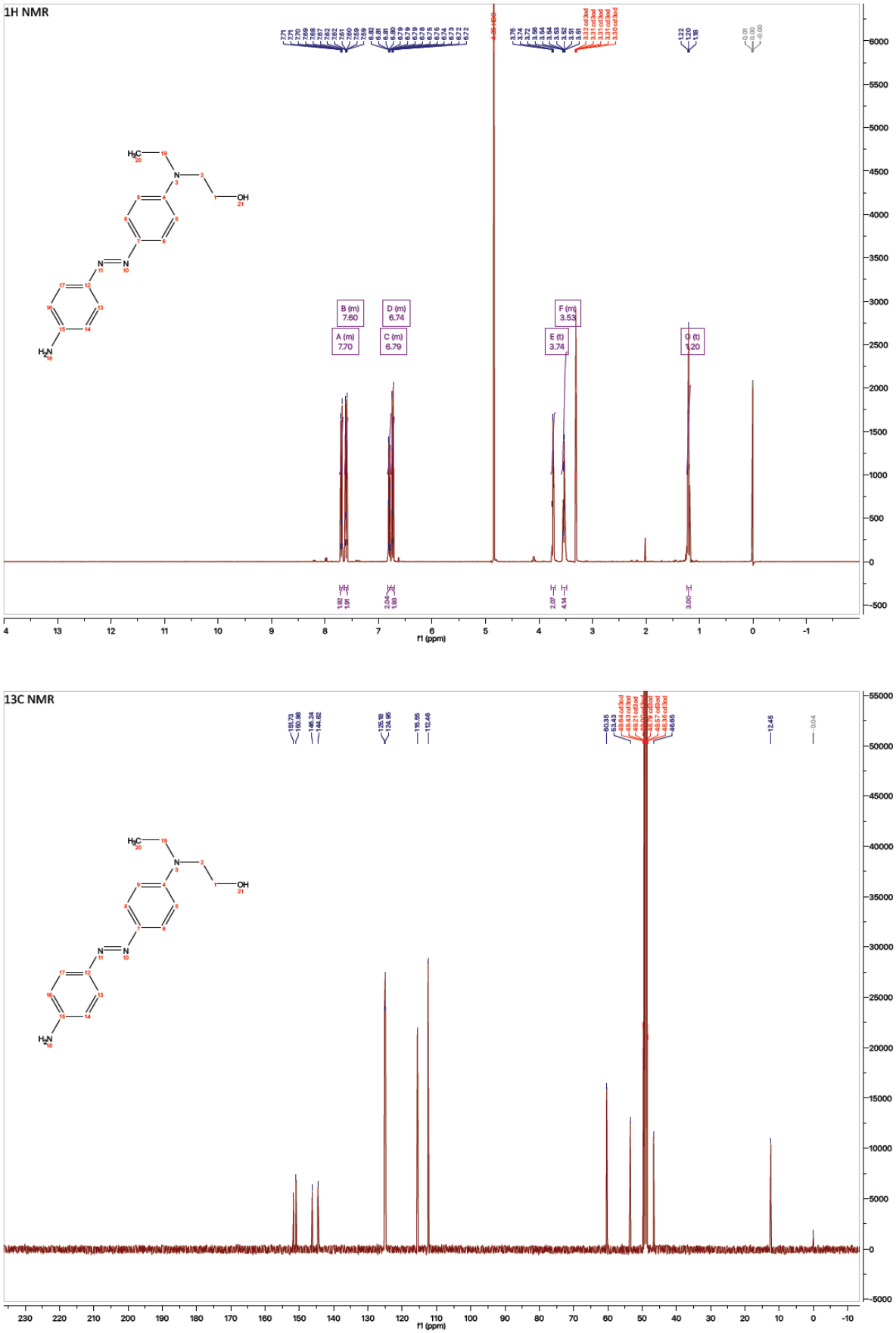

Figure S1. NMR spectra of compound **5**.

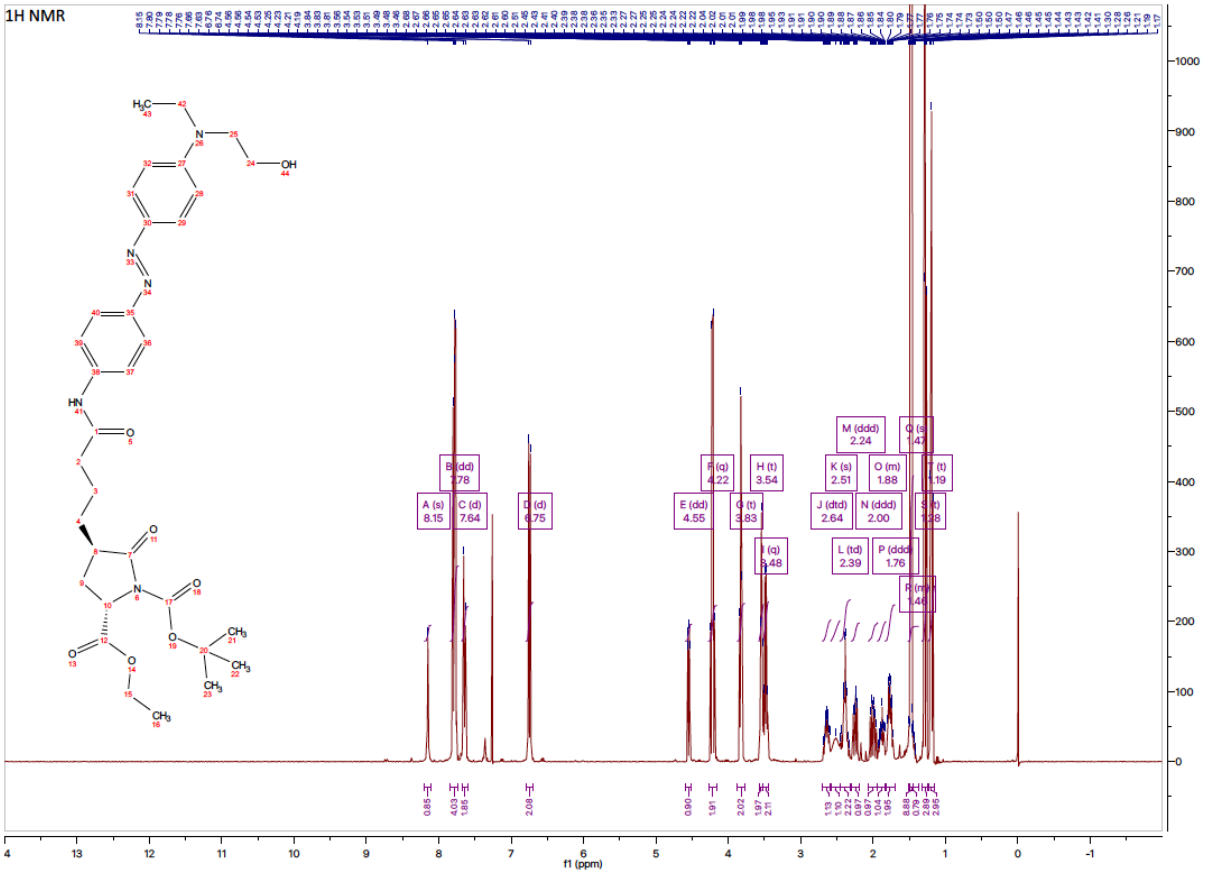

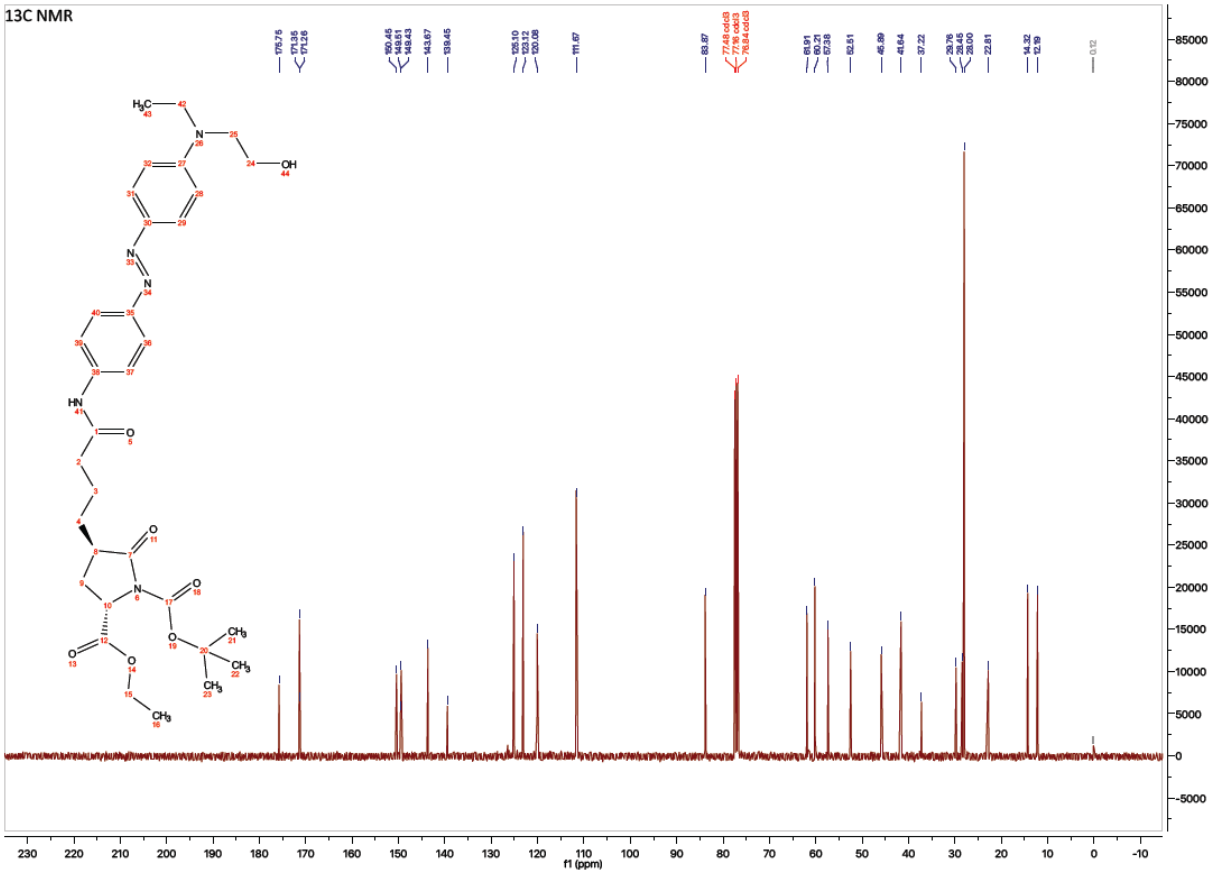

Figure S2. NMR spectra of compound **7**.

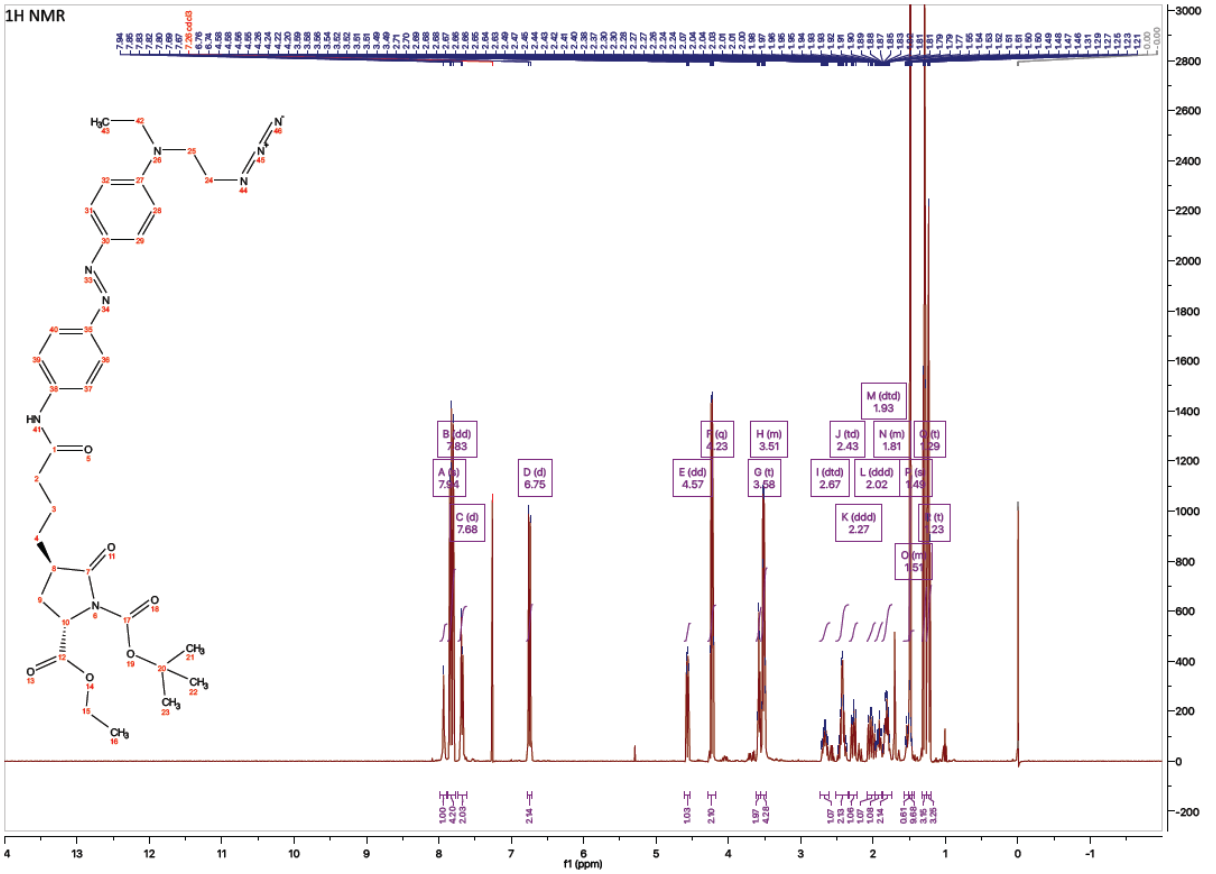

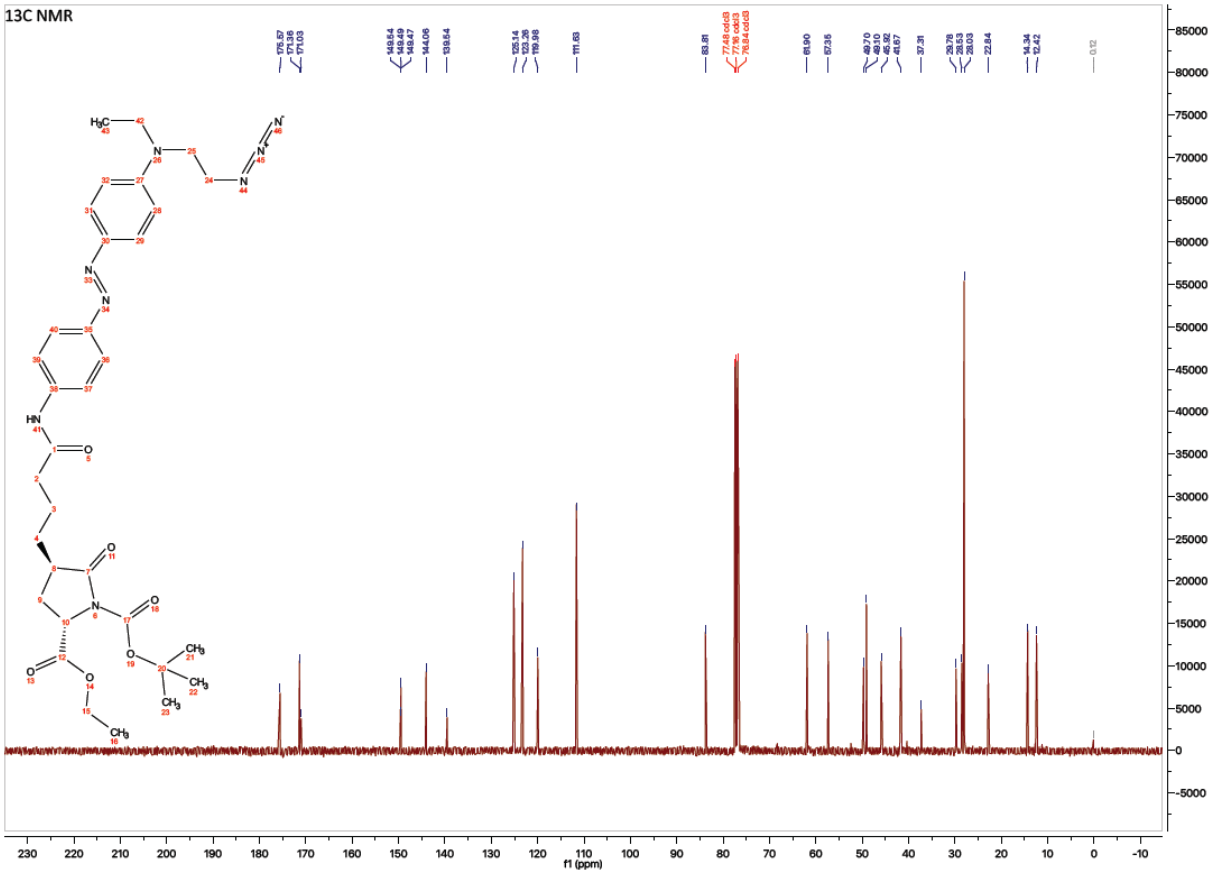

Figure S3. NMR spectra of compound **8**.

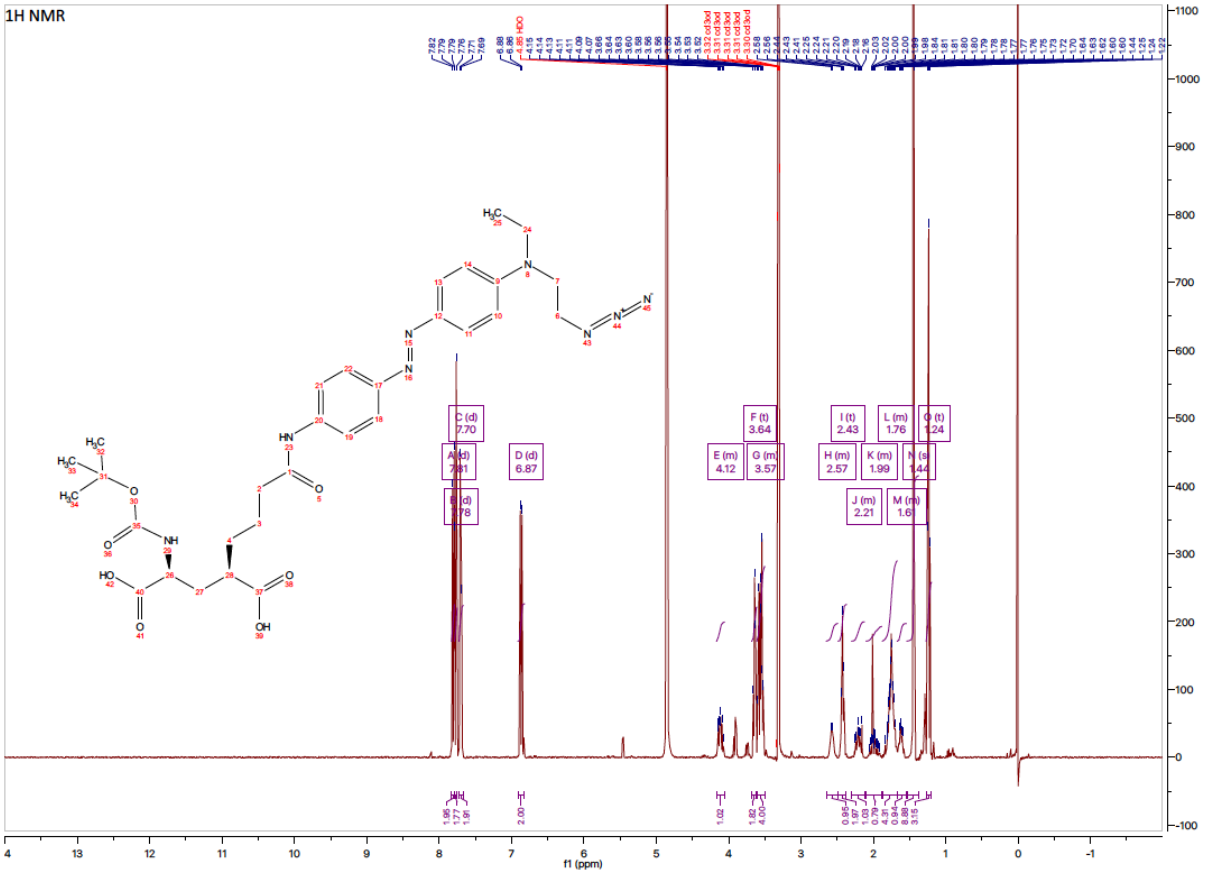

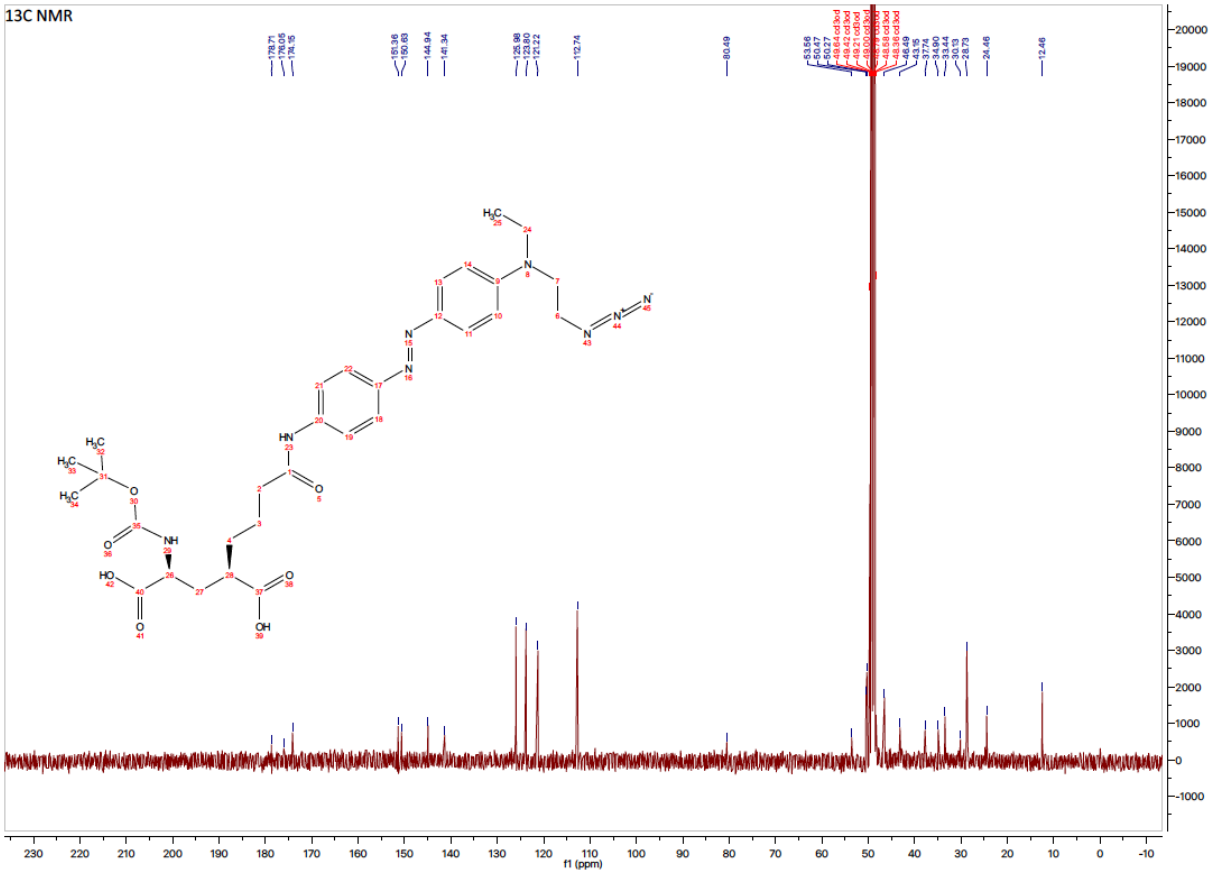

Figure S4. NMR spectra of compound **9**.

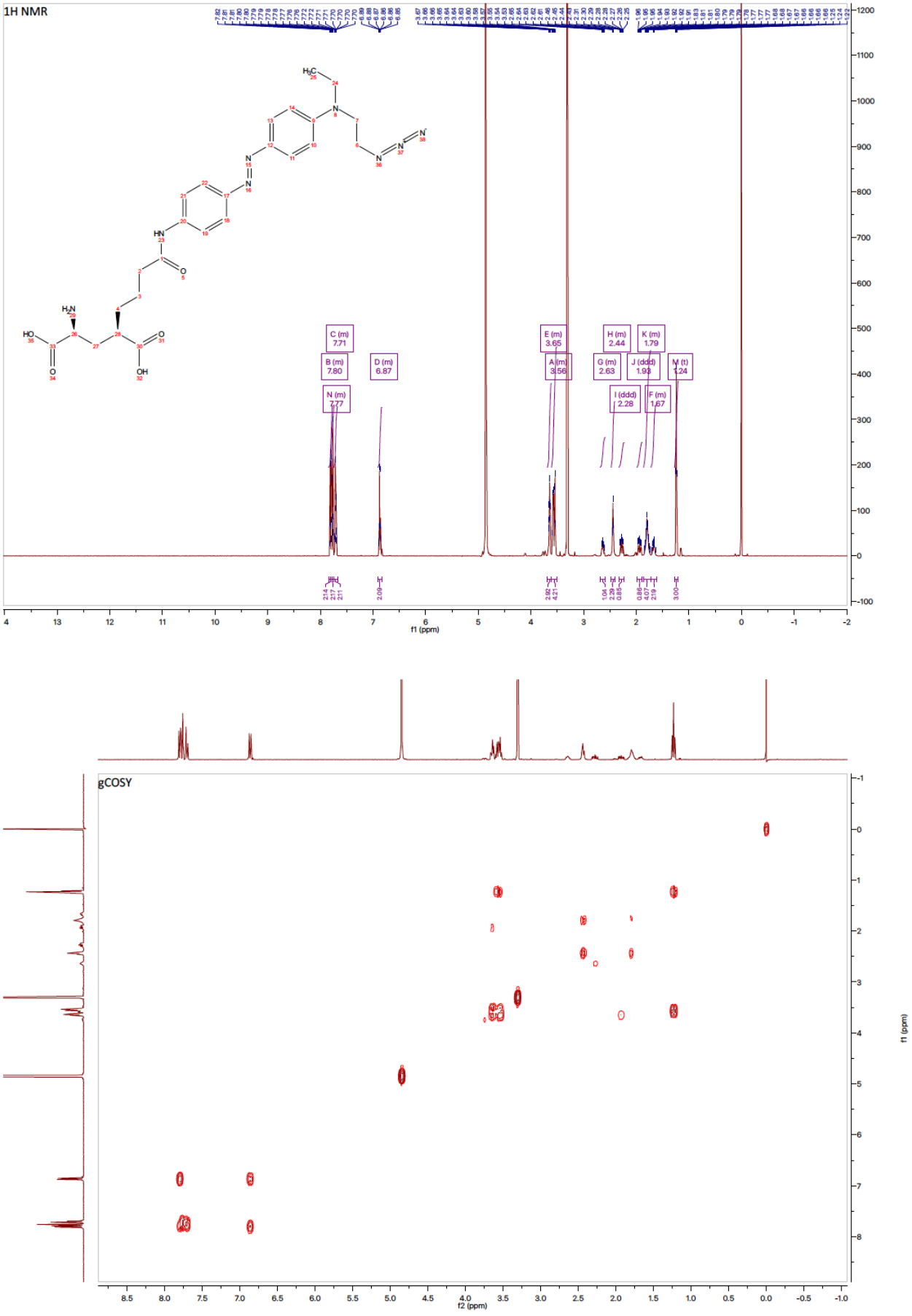

Figure S5. NMR spectra of compound **1** (continued to the next page).

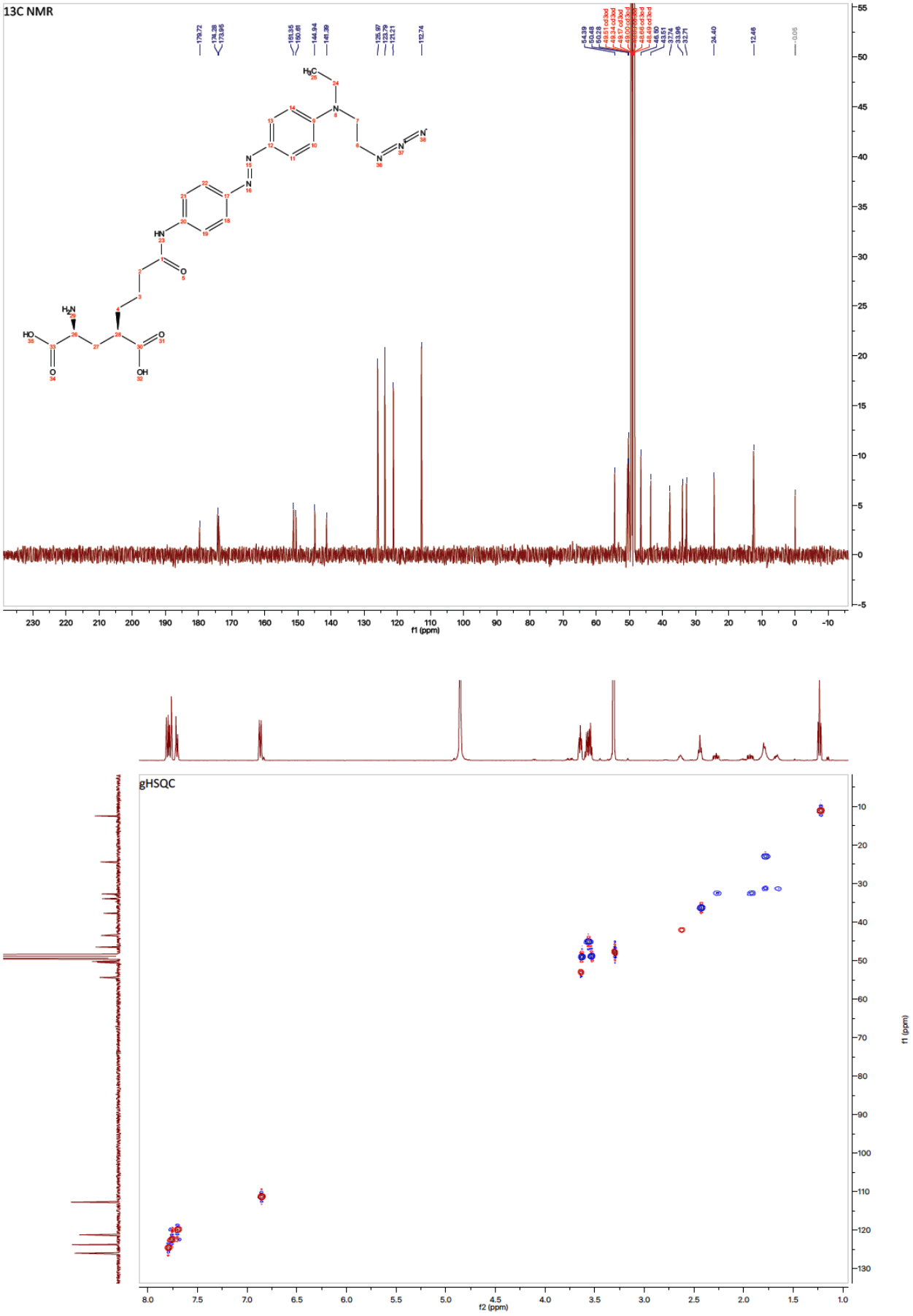

Figure S5. NMR spectra of compound **1** (continued from the previous page).

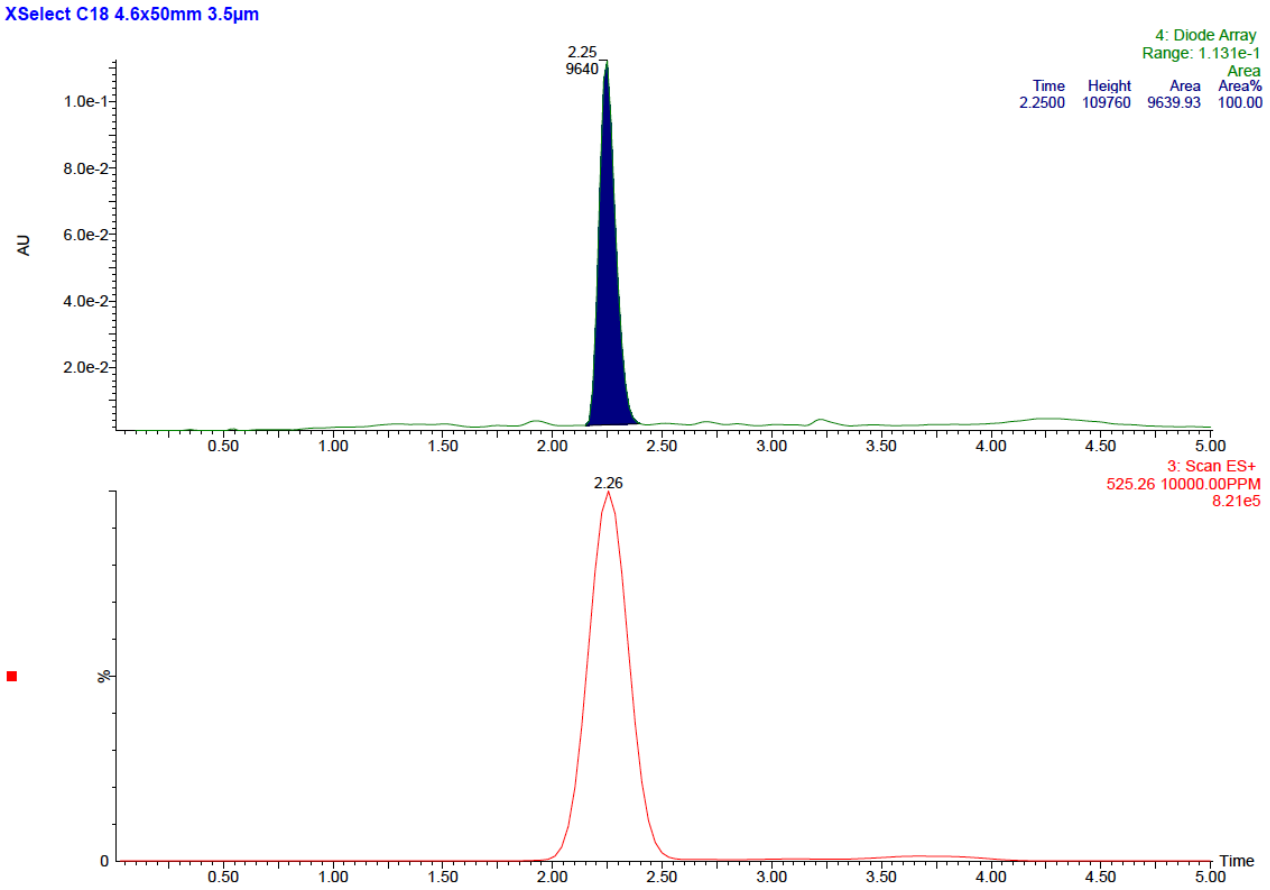

Figure S6. HPLC chromatogram of compound **1**.

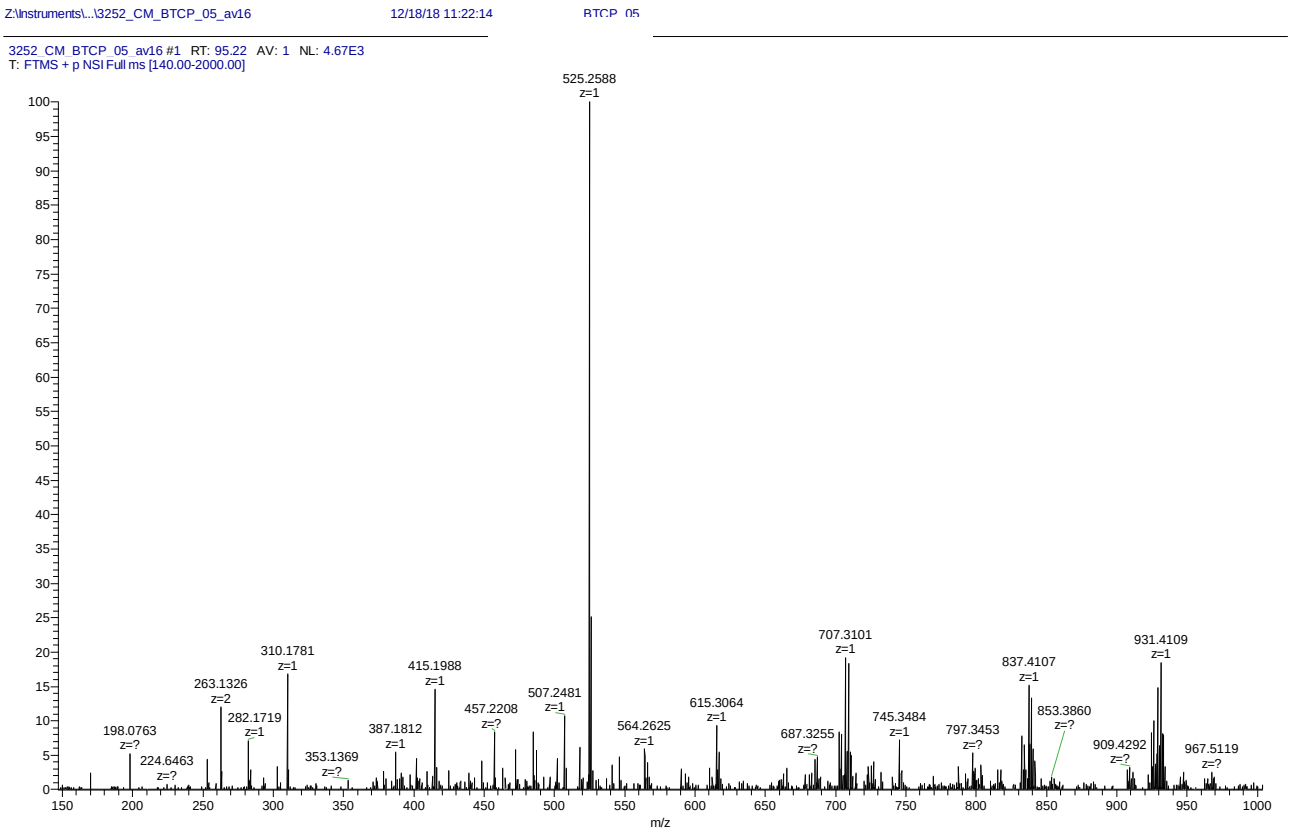

Figure S7. High-resolution mass spectrum of compound **1**.

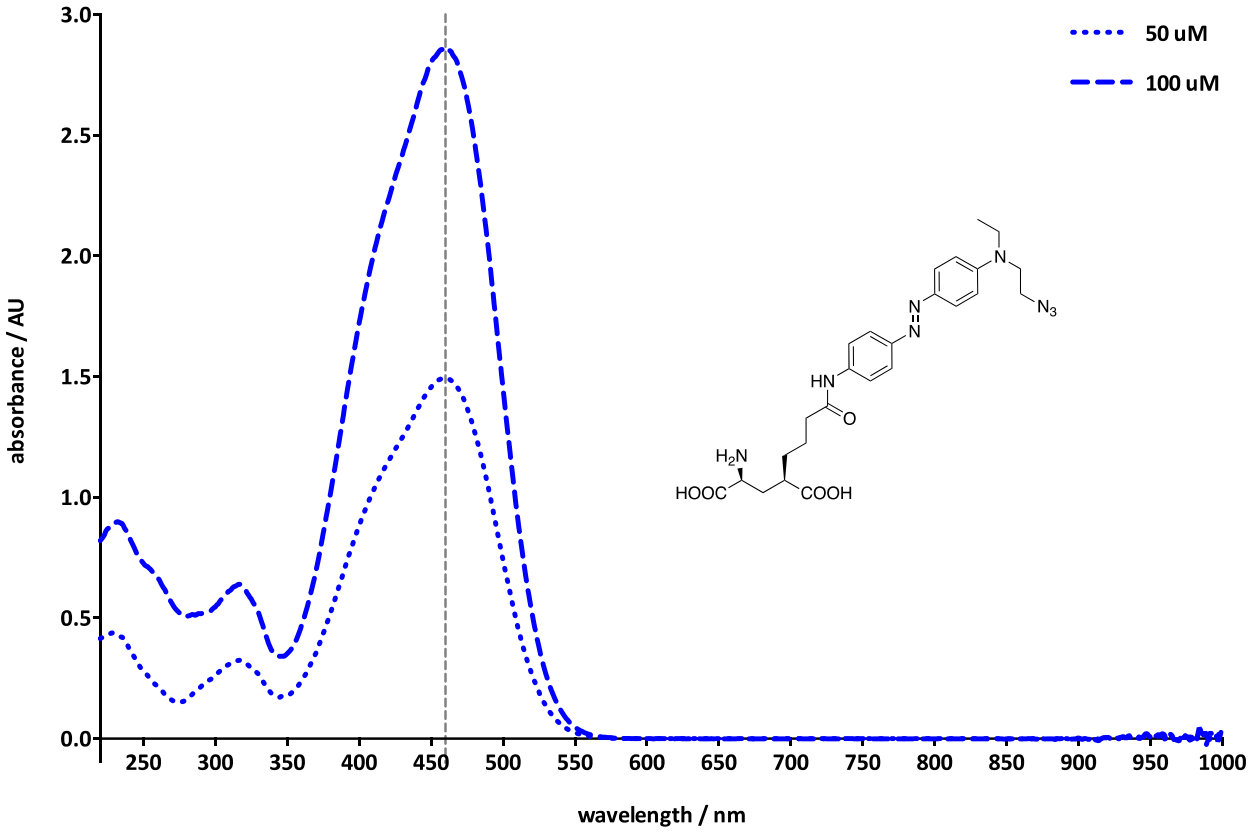

Figure S8. UV-Vis absorption spectrum of compound **1** (*trans* isomer) in PBS buffer at pH 7.4.

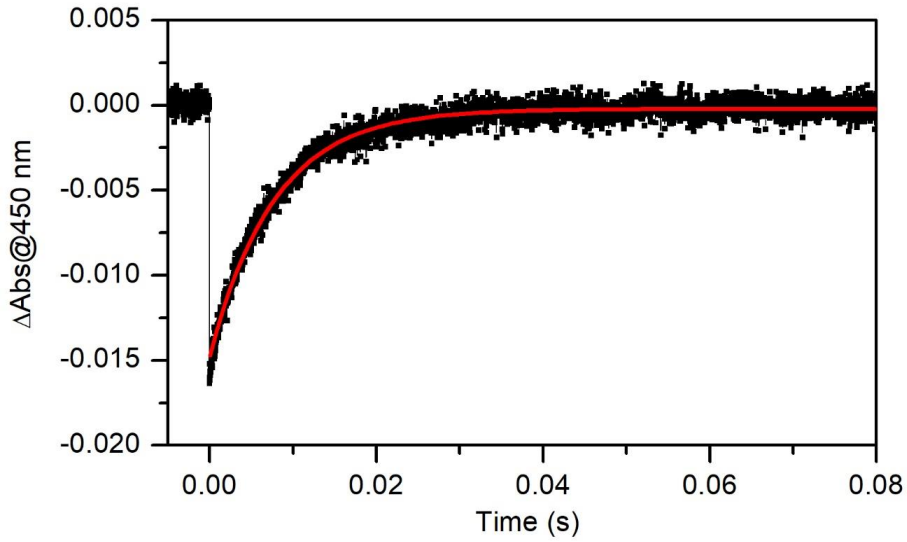

Figure S9. Photochromic behavior of compound **1** investigated by transient absorption spectroscopy. Variation of the absorption at λ_{abs} = 450 nm of **1** in PBS after irradiation of its initial *trans* state (27 µM) with a single ns laser pulse (*t* = 0) at λ_{exc} = 355 nm and 22 °C. The solid thick line corresponds to the monoexponential fit of the experimental data. The decay measured reports on the thermal back-isomerization in the dark of the *cis*-**1** molecules generated upon pulsed irradiation. From the monoexponential fit, a thermal lifetime of $\tau_{cis\text{-}1}$ = 7.7 ms was retrieved, which corresponds to a half-life of $t_{1/2,cis\text{-}1}$ = 5.3 ms.

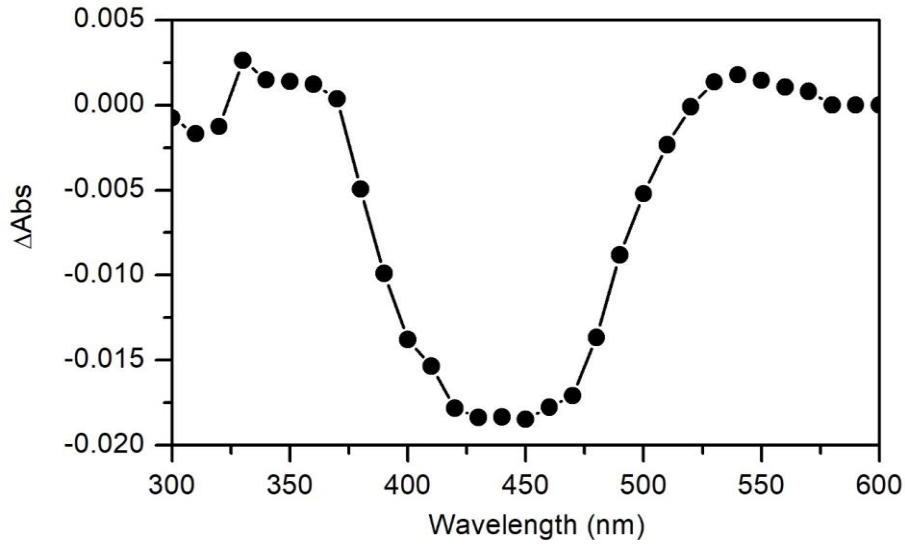

Figure S10. Transient absorption spectrum of compound **1**. Transient absorption spectrum at *t* = 0 of *trans*-**1** in PBS (27 µM) upon pulsed excitation at λ_{exc} = 355 nm and 22 °C. Because of the lower extinction coefficient of *cis*-**1** produced under irradiation, the spectrum shows a large negative bleaching signal that mirror-images the steady-state absorption spectra of *trans*-**1**.

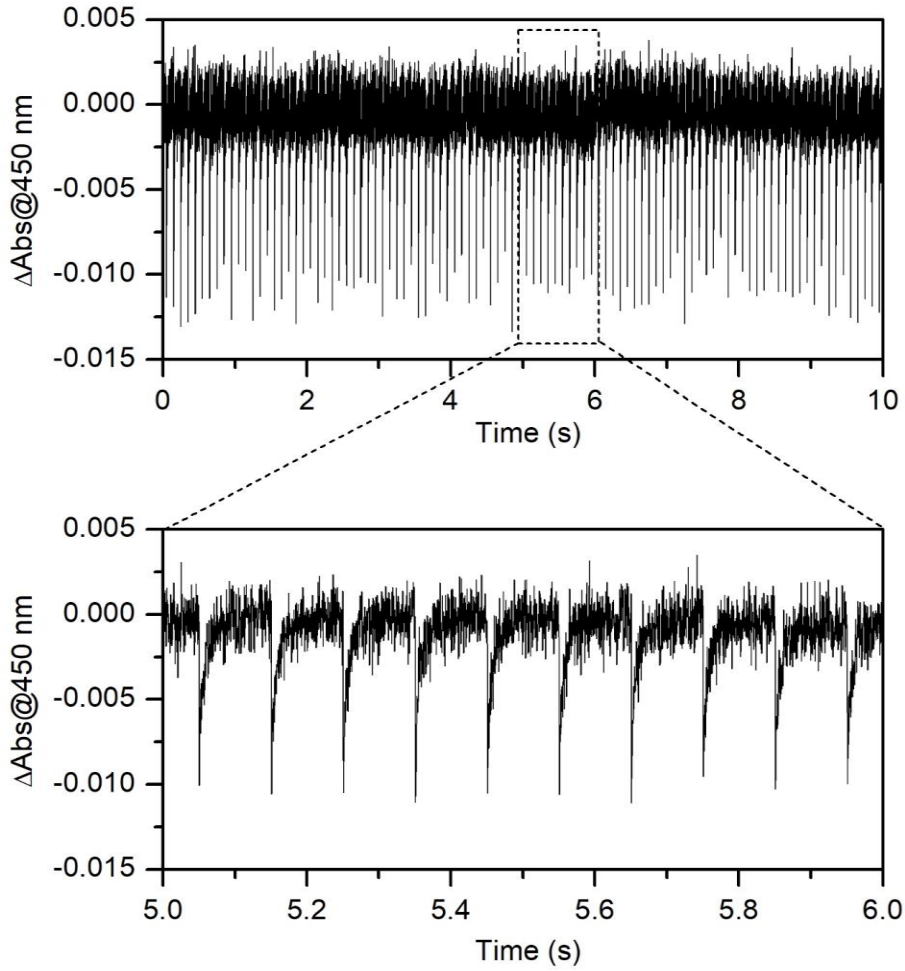

Figure S11. Photofatigue resistance of compound **1**. Transient absorption time traces measured for compound **1** in PBS (27 µM) at λ_{abs} = 450 nm and 22 °C upon excitation with a ns-pulsed laser at λ_{exc} = 355 nm and 10 Hz repetition rate. As shown in the inset, each laser pulse induces *trans-cis* isomerization of the irradiated compound, which subsequently relaxes back to the initial *trans* state thermally in less than 100 ms. After 100 *trans-cis* photoisomerization cycles, no significant photodegradation effects were observed.

4. Synthetic protocol for the preparation of TCP_{fast}

Head (**1**) and tail (**2**, commercially available) were combined to form the final TCP_{fast} (**3**) compound using a "click" version of the Huisgen azide-alkyne 1,3-dipolar cycloaddition[2]. Since such NHS-ester derivatives are very short-lived, we characterized the products of the click reaction crude of TCP_{fast} after subsequent reaction with pure L-lysine as a mock protein residue. Detailed analysis by LC-MS confirmed the presence of the intended TCP_{fast}–lysine adduct with an intact glutamate moiety and of some of the expected byproducts.

General procedure. To a 1.5 ml glass vial containing azide **1** ('head', 1.00 mg, 1 eq) and copper(I) oxide (0.82 mg, 3 eq) in tetrahydrofuran (47 µL) and equipped with a magnetic stir bar was added a solution of ascorbic acid (1.34 mg, 4 eq) in water (94 µL) and the resulting mixture was vortexed for 1 min. Then, a solution of alkyne **2** ('tail', 0.47 mg, 1.1 eq) in tetrahydrofuran (47 µL) was added and the resulting mixture was stirred at room temperature for 45 min. The so-obtained final mixture was taken up in dimethylsulfoxide (193 µL), vortexed, centrifuged for 1 min to separate the insoluble copper(I) oxide particles, and finally divided into aliquots of the final compound stock solution (Scheme S2).

Alternatively, the click reaction could be performed in an Eppendorf tube and stirred with a suitable mixer.

We observed that the catalytic performance of the copper(I) oxide may vary significantly from batch to batch, therefore the actual reaction time should be adjusted accordingly in order to obtain a ≥95% conversion of the starting material and a (TCP_{fast}):(hydrolyzed TCP_{fast}) ratio greater than 3 (Figure S12).

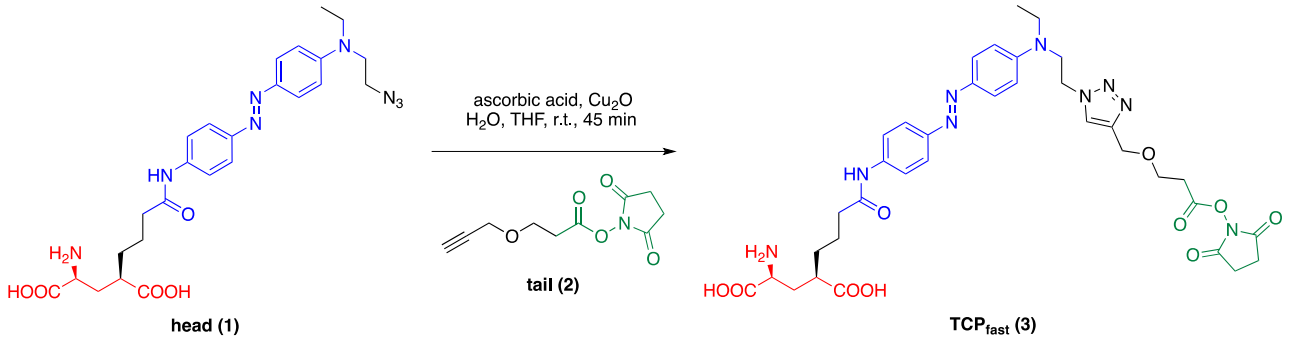

Scheme S2. Preparation of TCP_{fast} via Cu(I)-catalyzed azide-alkyne 1,3-dipolar cycloaddition reaction.

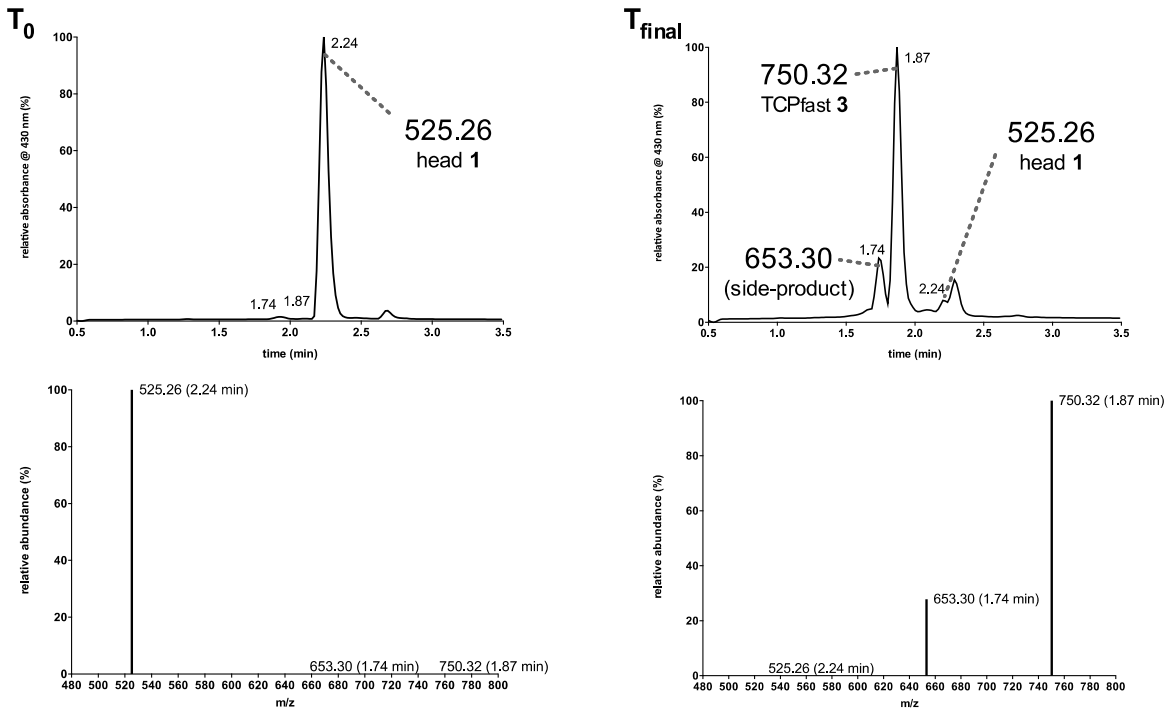

Figure S12. Analysis of the initial and final mixture of a representative "click" reaction for the preparation of TCP_{fast} (**3**), showing the conversion of the starting material to the final desired product and its side-product [top: HPLC chromatograms; *y*-axis shows relative absorbance (%) at 430 nm; bottom: selected ion recording (SIR) of the corresponding HPLC chromatograms for head (**1**), TCP_{fast} (**3**) and its major side-product; *y*-axis shows relative abundance (%) of the ion species; see also Scheme S3 for further details].

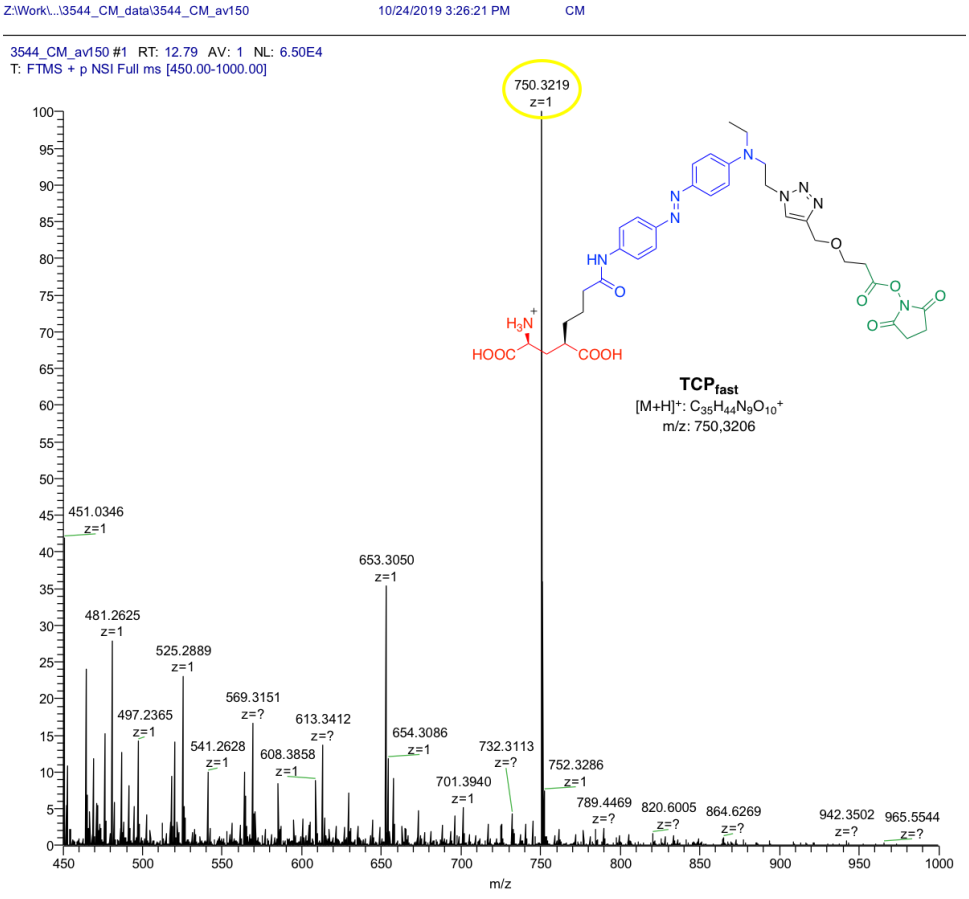

Figure S13. High-resolution mass spectrum of TCP_{fast} (**3**).

5. Characterization of TCP_{fast}, lysine-adduct, and side-product by LC-MS

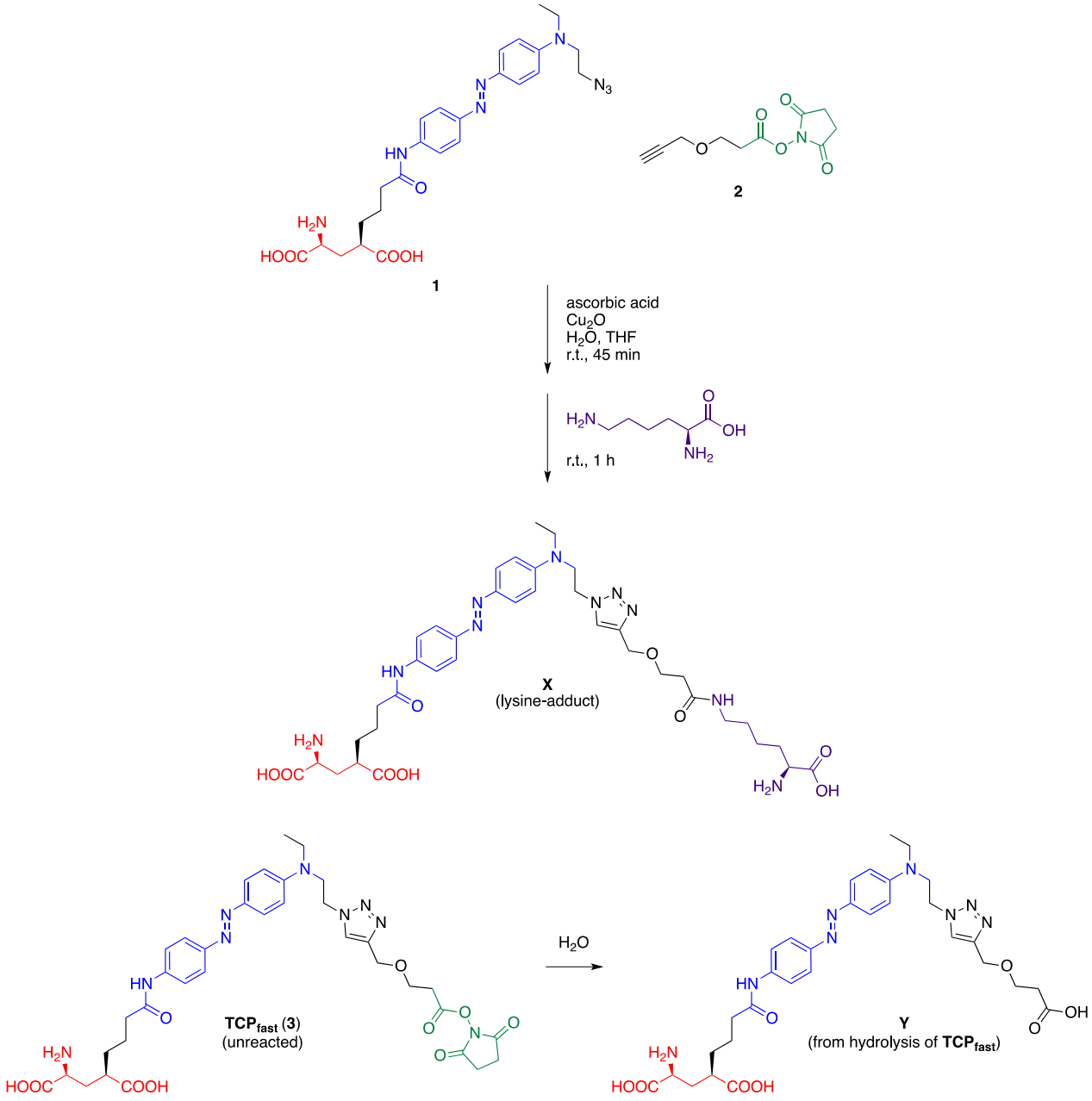

Scheme S3. Generation and structure of TCP_{fast}–lysine adduct (**X**) and detected major side-product (**Y**).

Compound	*m/z* calculated for $[M+H]^+$	*m/z* calculated for $[M+2H]^{2+}$
1	$C_{25}H_{33}N_8O_5^+$: 525.26	$C_{25}H_{34}N_8O_5^{2+}$: 263.13
TCP_{fast} (3)	$C_{35}H_{44}N_9O_{10}^+$: 750.32	$C_{35}H_{45}N_9O_{10}^{2+}$: 375.66
X	$C_{37}H_{53}N_{10}O_9^+$: 781.40	$C_{37}H_{54}N_{10}O_9^{2+}$: 391.20
Y	$C_{31}H_{41}N_8O_8^+$: 653.30	$C_{31}H_{42}N_8O_8^{2+}$: 327.16

Table S1. Calculated mass-to-charge (*m/z*) ratio for compounds **1**, TCP_{fast} (**3**), **X**, **Y**.

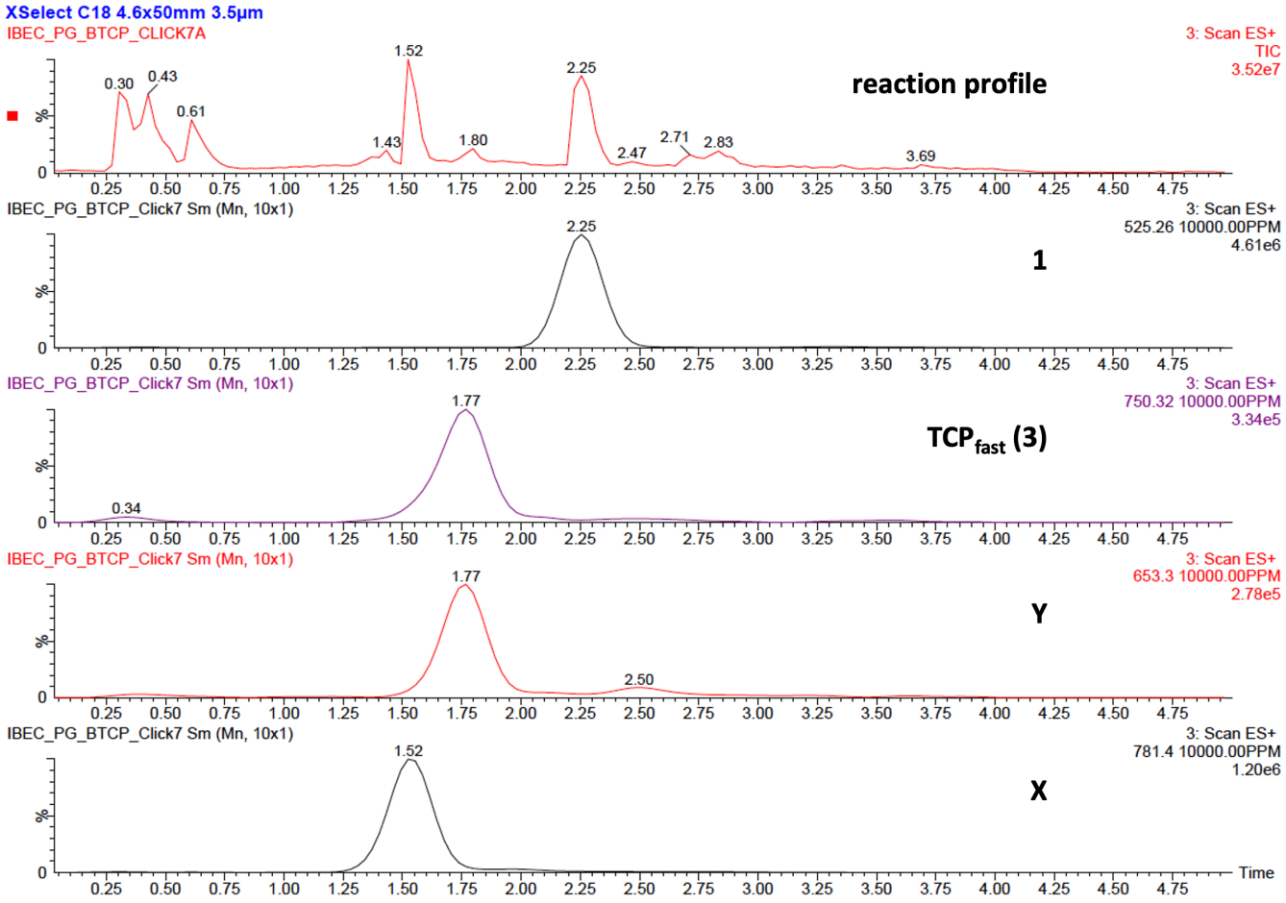

Figure S14. LC-MS analysis of the final mixture for the reaction in Scheme S3 (arbitrary case).

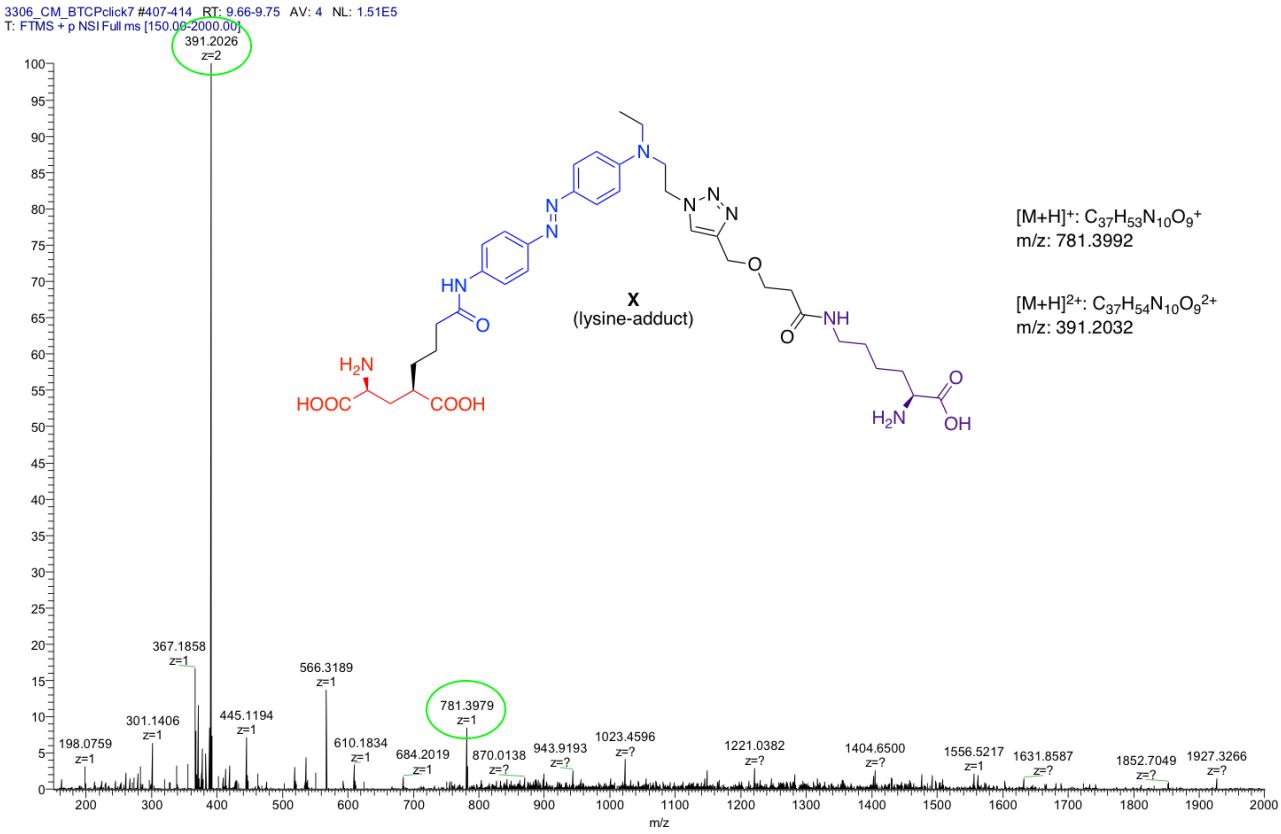

Figure S15. High-resolution mass spectrum of TCP_{fast}–lysine adduct (**X**).

6. Characterization of TCP_{fast} in cultured neurons

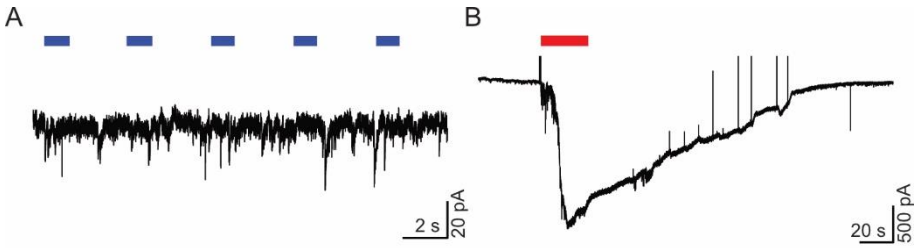

Figure S16. Light stimulation does not affect neuronal responses prior to TCP_{fast} incubation. A. Hippocampal neurons non-incubated with TCP_{fast} do not respond to light (473 nm for 1 s, blue bars). **B.** Physiological responses to glutamate perfusion (300 µM, red bar) indicate expression of glutamatergic receptors.

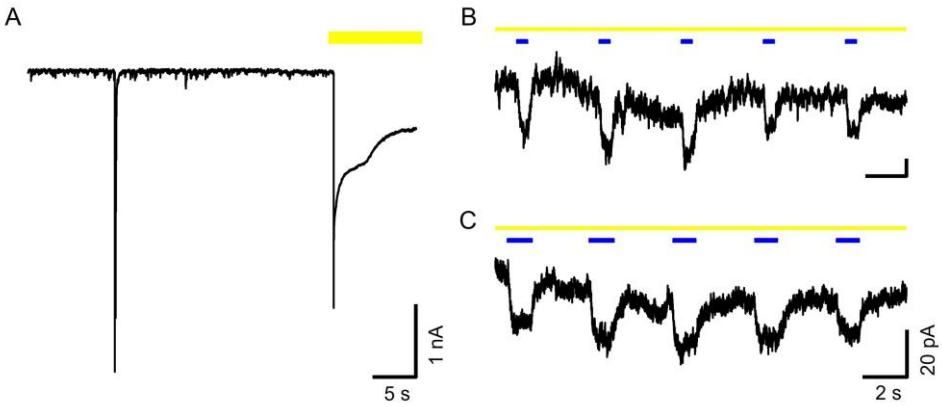

Figure S17. Light-independent effect of free-diffusible TCP_{fast}. A. Direct perfusion of TCP_{fast} in the dark in dissociated hippocampal neurons (100 µM, pH 7.4) demonstrates that *trans*-TCP_{fast} can activate glutamate receptors as free glutamate and this effect can be enhanced by blue light activation. This also indicates that in the dark, the glutamate moiety is the first part to interact with the ligand binding domain prior to TCP_{fast} conjugation. **B.** Light pulses of 500 ms (blue bars) in presence of TCP_{fast} (yellow bar). **C.** Light pulses of 1 s.

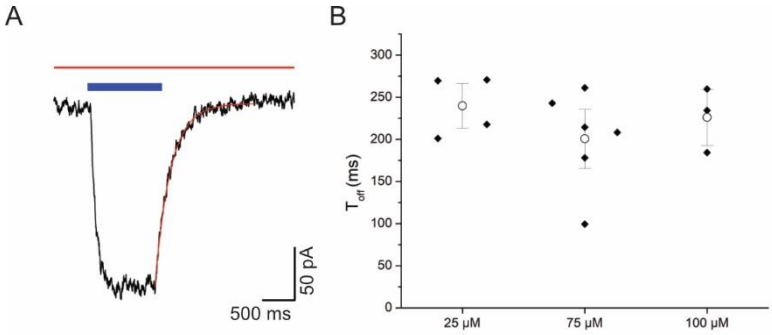

Figure S18. Fast relaxation lifetime of TCP_{fast} enables single wavelength control of photocurrents in hippocampal neurons. A. Representative current recording in response to 1 s blue light stimulation (blue bar) in presence of glutamate (300 µM, red bar) in bath solution. Whole cell voltage clamp mode recording in rat hippocampal neuron maintained 15 days in culture and incubated with TCP_{fast} (100 µM for 2 min at pH9). Exponential fit of the photocurrent to obtain T_{off} is showed in red. **B.** T_{off} average values obtained in neurons incubated with TCP_{fast} for 2 min at pH 9 at 25 µM (n=4), 75 µM (n=6) and 100 µM (n=3). Each data point is the average of T_{off} values obtained from fitting 5 different light pulses in the same cell. White dot is mean ± SE. The relaxation lifetime averaged for all concentrations is 220 ± 48 ms.

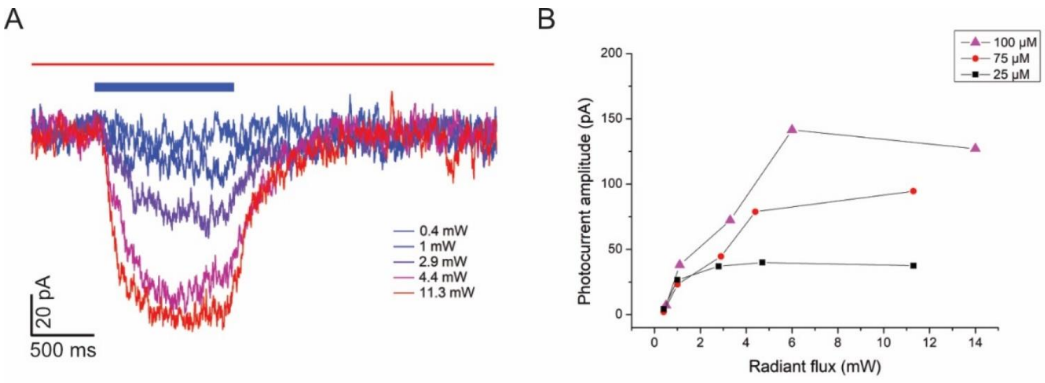

Figure S19. Photocurrent amplitude depends on light intensity. A. Superimposed representative photocurrent responses to different light intensities (473 nm, 1 s) in the same neuron. Power values are indicated in the label. Whole cell voltage clamp mode recording in dissociated rat hippocampal neurons maintained 12 days in culture and incubated with TCP_{fast} (75 µM for 2 min at pH9). **B.** Photocurrent amplitude as a function of radiant flux of different neurons incubated at different concentrations of TCP_{fast} for 2 min at pH9.

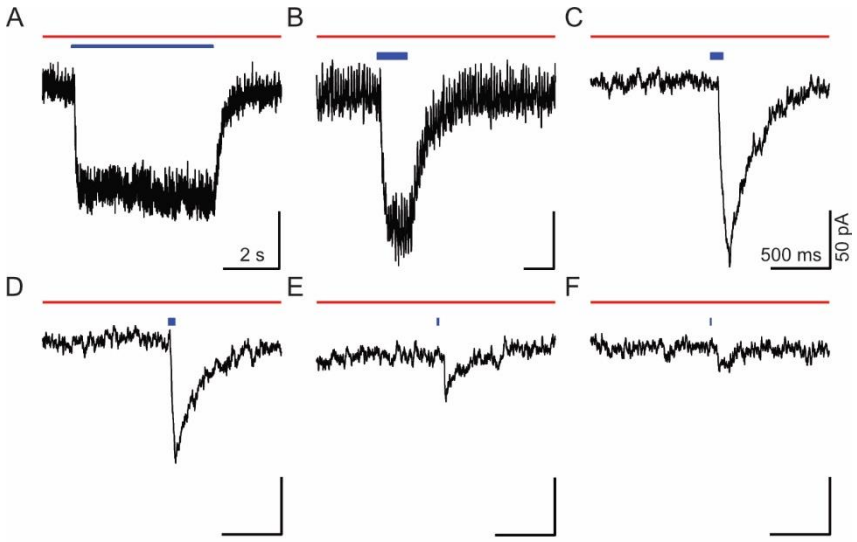

Figure S20. Neurons incubated with TCP_{fast} display reversible *cis*-on photocurrents in response to blue light pulses as short as a few milliseconds. Current recording in whole cell voltage clamp mode of dissociated rat hippocampal neurons maintained 15 days in culture and incubated with TCP_{fast} (100 µM for 2 min at pH9). Photocurrents elicited by illumination at λ_{ex} = 473 nm and duration 5 s (A), 500 ms (B), 100 ms (C), 50 ms (D), 10 ms (E) and 3 ms (F) in the presence of 300 µM glutamate (red bar).

7. *In vivo* photocontrol of neural activity in gerbil's cochlea

Supporting Method S1: Cochlear mass potentials

Using a silver ball electrode placed into the niche of the round window (RW, i.e. one of the two openings into the cochlea, Figure 3A-B), acoustically and optically evoked cochlear mass potentials were recorded. The acoustically evoked cochlear mass potential contains the electrophysiological response of three cochlear cell types involved in the transduction of sound to an electric signal, which can be isolated by filtering: *i*) the cochlear microphonic (Figure S21A$_3$) reflecting the activation of the outer hair cells, responsible for amplification of sound-borne cochlear vibrations [3]. It is extracted by applying a low-pass filtering to the mass potential (< 3.5 kHz) and it corresponds to the positive plateau response following the negative N_1 and positive waves P_1; *ii*) the summating

potential (Figure S21A$_4$) reflecting mainly the activation of the inner hair cells, responsible of synaptic sound encoding [4] and extracted by applying a band-pass filter centered on the tone burst frequency.; *iii*) the compound action potential (Figure S21A$_4$) reflecting the synchronous firing of action potentials by the spiral ganglion neurons. It is extracted by applying a low-pass filtering to the mass potential (< 3.5 kHz) and it corresponds to the negative N_1 waves. In response to optical stimulation using TCP_{fast}, the compound action potential is the only expected mass potential.

Supporting Method S2: Evaluation of the excitotoxicity by counting the number of inner hair cell synapses

In cochlear hair cells, excitotoxicity is characterized, in electron microscopy images, by a massive swelling of the postsynaptic bouton characterized by an absence of cytoplasmic content[5]. Acoustic trauma is a classical model of glutamate excitotoxicity and is characterized by an acute and permanent loss of the postsynaptic structure facing an intact presynaptic ribbon, visualized in confocal microscopy images[6]. In both cases, the synaptic damages were already visible within minutes of glutamate overexposure [5,7]. Therefore, in this study to evaluate if TCP_{fast} was associated with excitotoxicity, we quantified the number of synapses at different cochlear positions for control and treated cochleae within two hours following TCF_{fast} application. We defined synapses by the juxtaposition of a presynaptic protein, CtBP2, and a postsynaptic protein, Homer1. The number of reported synapses is similar between both groups and previously published data [8,9].

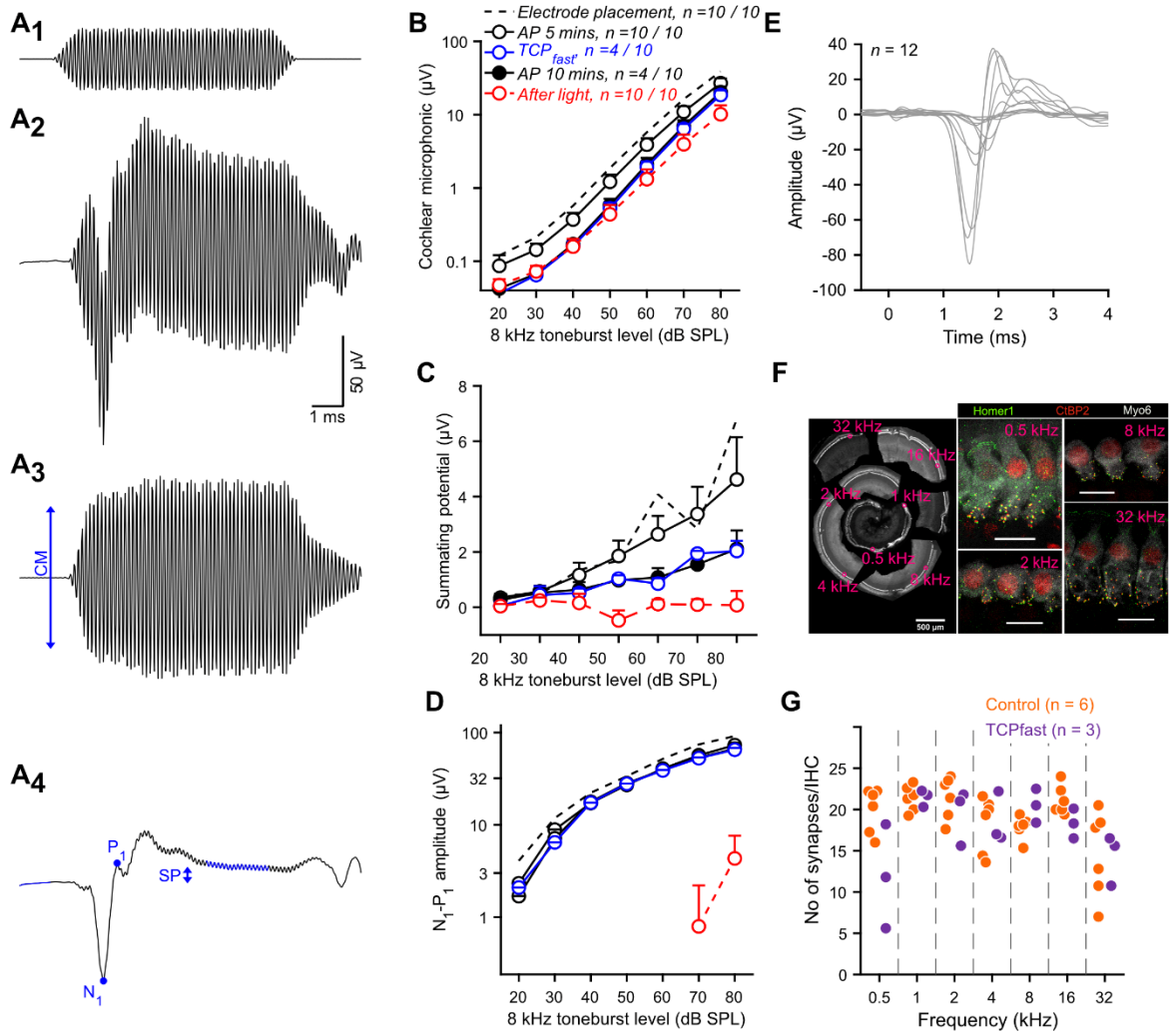

Figure S21. 12.5 µM TCP_{fast} administration into the cochlea enables a transient optically evoked response of the SGNs followed by a loss of function of the inner hair cells and spiral ganglion neurons. A. Cochlear mass potentials (A$_2$),

recorded by a silver ball electrode implanted into the cochlear round window niche, in response to acoustic toneburst of 8 kHz (A_1). The cochlear microphonic (CM, A_3), reflecting outer hair cells activity, is extracted from the mass potential by a band passed filter centered on the stimulation frequency. The summating potential (SP, A_4), reflecting inner hair cell activity, is measured as the difference between the base line and the plateau potential of the low-passed (< 3.5 kHz) filtered mass potential. The compound action potential (CAP, A_4), reflecting the synchronous SGN first spike evoked by the sound stimulation, is measured as the difference between the negative peak N_1 and the positive peak P_1. **B-D.** Quantification (mean ± SEM) of the cochlear microphonic (B), summating potential (C) and CAP (D) as a function of the stimulation level after electrode placement (dashed line, *n* = 10), 5 min after artificial perilymph (AP) application defining the base line (open black circle, *n* = 10), following 12.5 µM TCP_{fast} application (open blue circle, *n* = 4), 10 min rinsing with AP (close dark circle, *n* = 4) and following light stimulation (red open circle, *n* = 10). **E.** Transient optically evoked CAPs (oCAP) recorded from 12 treated cochleae with 12.5 µM TCP_{fast}. **F.** Right: Maximum projections of confocal stacks of immunolabelled gerbil IHC afferent synapses (IHC, anti-Myo6, gray; pre-synapse, anti-CtBP2/RIBEYE, red; post-synapse, anti-Homer1, green) at different tonotopic location (scale bar = 10 µm). Left: Montage of the low-magnification view of fragments of the full gerbil organ of Corti (scale bar = 500 µm). **G.** Quantification of the number of synapses per IHC between non-treated (*n* = 6) and 12.5 µM TCP_{fast} treated (*n* = 3) cochleae at different tonotopic regions (0.5, 1, 2, 4, 8, 16 and 32 kHz).

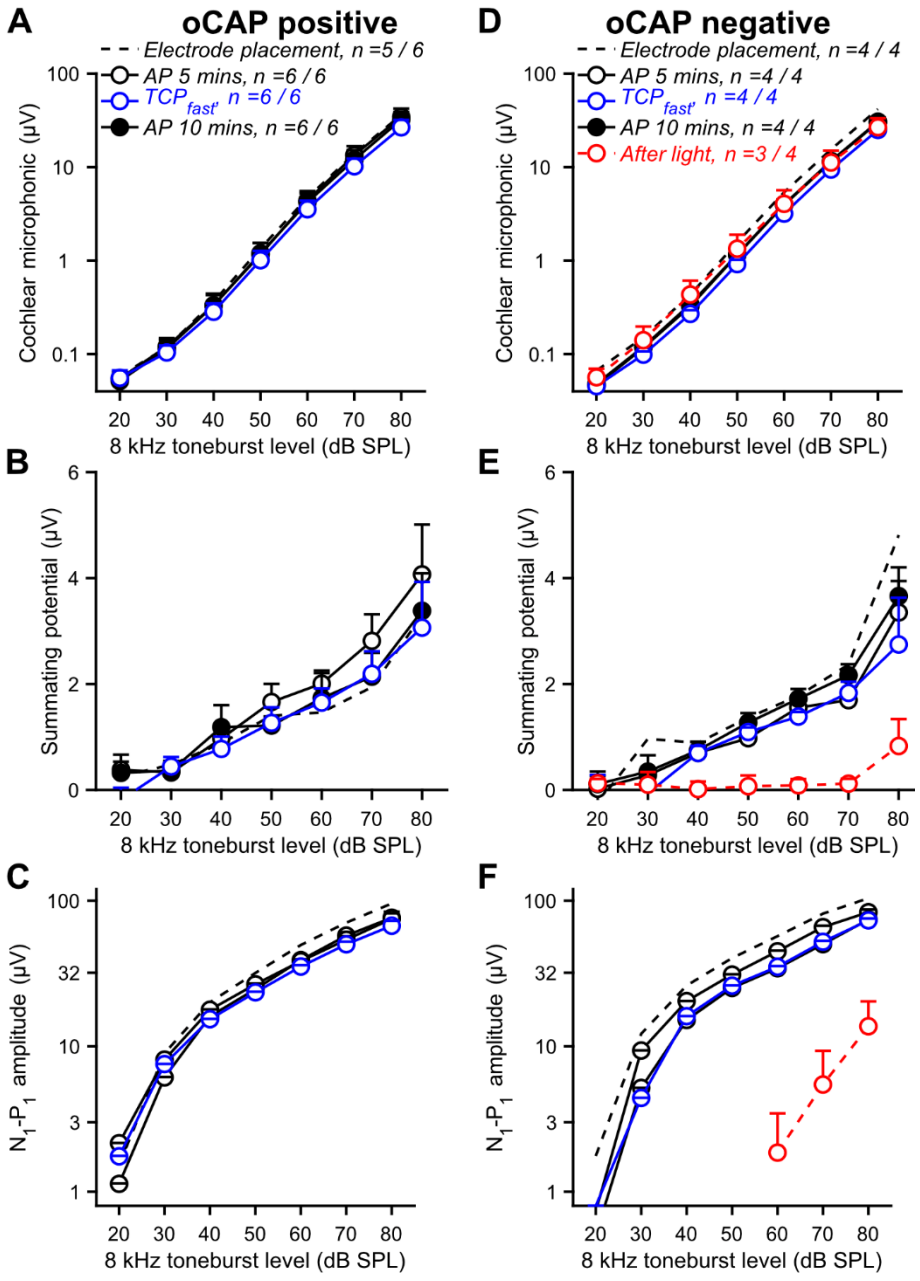

Figure S22. In 60% of the cases 2.5 µM TCP_{fast} application into the cochlea allows stable photoresponse in absence of toxicity for the organ of Corti. A-F. Quantification (mean ± SEM) of the cochlear microphonic (A,D), summating potential

(B,E) and CAP (C,F) as a function of the stimulation level after electrode placement (dashed line), 5 min after artificial perilymph (AP) application defining the baseline (open black circle), following 12.5 µM TCP_{fast} application (open blue circle), 10 min rinsing with AP (close dark circle) and following light stimulation (red open circle) for the cochleae from which stable optically evoked CAPs were recorded (oCAP positive) or not (oCAP negative).

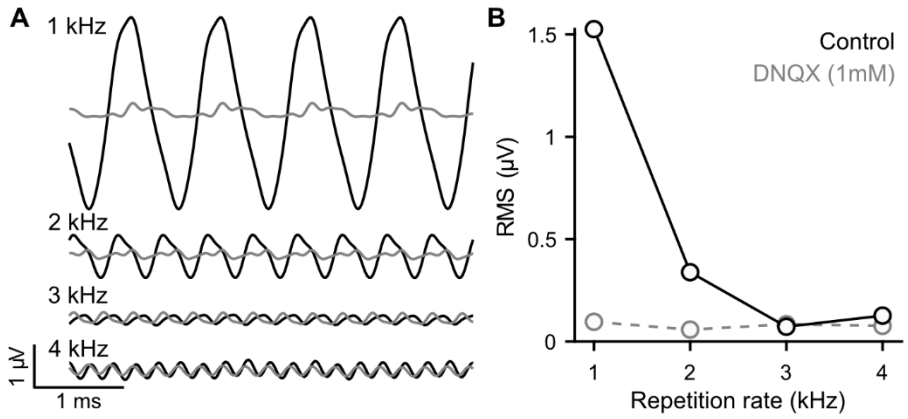

Figure S23. TCP_{fast} enables oCAPs up to stimulation rate of 2 kHz. A. oCAPs recorded from one cochlea in response to 1, 2, 3 and 4 kHz repetition rate before (black) and after DNQX (1 mM, gray). **B.** Measure of the oCAP amplitude (illustrated in A) as a function of the repetition rate before (black) and after DNQX application (gray).

8. Sequence alignment and molecular docking simulations

Ligand binding domain sequence alignments of Kainate and AMPA receptors

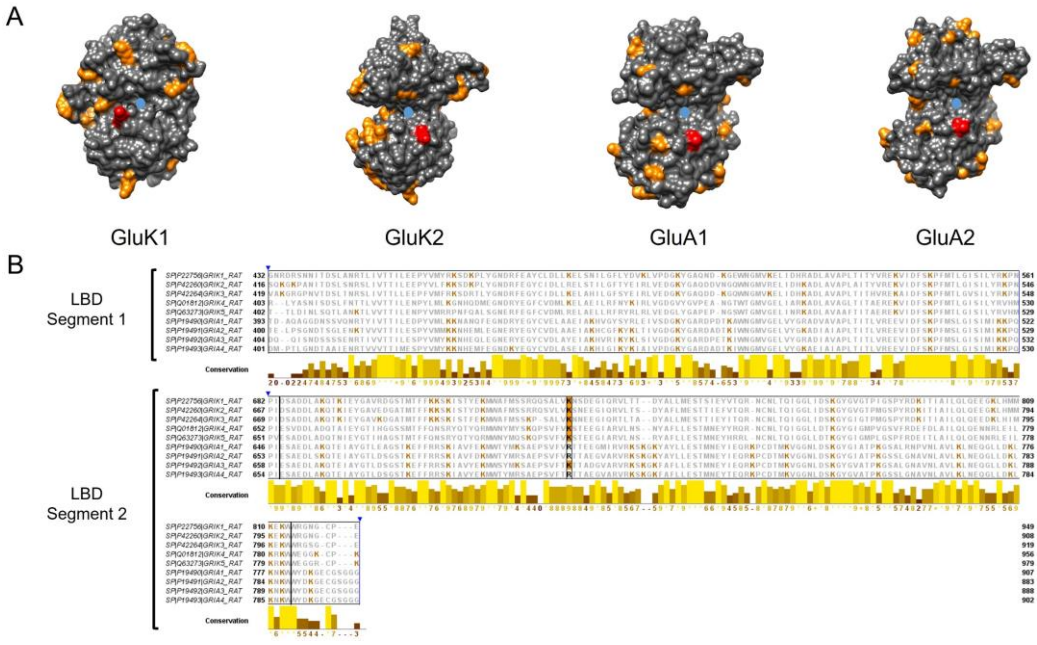

Figure S24. Comparison of Kainate and AMPA receptor ligand binding domains show putative anchoring residues. A. Structure of the ligand binding domain of GluK1 (PDB 1TXF), GluK2 (PDB 7F56), and GluA1/A2 (PDB 6QKC). The main residue targeted by TCP9 and TCP10 in GluK1, Lys 734 [10] is highlighted in red in the GluK1 structure, and its homologous position is indicated in the other iGluRs. Other exposed basic residues of the ligand binding domains around the glutamate binding pocket are shown in orange. The glutamate binding pocket entry is indicated with a blue dot. **B.** Ligand binding domain sequence segment 1 and 2 from *R. norvegicus* genes encoding for GluK1 (P22756), GluK2 (P42260), GluK3 (P42264), GluK4 (Q01812), GluK5 (Q63273), GluA1 (P19490), GluA2 (P19491), GluA3 (P19492) and GluA4 (P19493). Sequences were aligned using Uniprot alignment tool and displayed using Jalview[11]. The alignment shows previously identified Lys734 in GluK1 is conserved in GluK2 and conservatively replaced in GluA1/A2. Lys734 is highlighted in orange box. Lysines are text colored orange.

Molecular Docking Simulations

Materials & Methods. Molecular docking simulations were performed with the AutoDock Vina tool[12] implemented in UCSF Chimera 1.16[13] using the crystal structure of the GluA2 agonist binding domain (PDB 5FHM). The protein pdb file was prepared for docking using the Dock Prep tool implemented in the software (default settings). All co-crystallized ligands, non-complexed ions, and water molecules were removed. The structures of TCP_{fast} (*trans* and *cis*) were built with standard bond length and angles using ChemDraw 20.1 and then prepared for docking using the Dock Prep tool (default settings). Docking simulations were carried out using the standard docking protocol applied for AutoDock Vina in UCSF Chimera 1.16 (number of binding modes = 10, exhaustiveness of search = 8, maximum energy difference = 3 kcal/mol). A grid box of size 25 × 25 × 25 Å with coordinates x = 0.65, y = -10.10 and z = 19.20 was fixed to cover the entire binding site while forcing at the same time the TCP_{fast} tail bearing the NHS ester anchoring group in proximity of the protein surface. All rotatable bonds within the ligands were allowed to rotate freely, while the protein was considered rigid. Docking simulations were repeated at least three times for each isomer. The obtained docking poses were selected by visual inspection based on the orientation of the glutamate moiety and ranked by predicted affinity docking scores (kcal/mol). All results were analyzed using UCSF Chimera.

Results & Discussion. Molecular docking simulations were performed to identify potential conjugation sites of TCP_{fast} at the AMPA receptor. For this purpose we used the crystal structure of the agonist binding domain of GluA2 (PDB 5FHM)[14], that appears to be expressed at every synapse in spiral ganglion neurons[15]. Dimensions and position of the grid box (receptor search volume) were arbitrarily chosen in order to cover the entire binding site while forcing at the same time the TCP_{fast} tail bearing the NHS ester anchoring group in proximity of the protein surface. Docking simulations were repeated at least 3 times for each isomer, and the obtained poses were selected by visual inspection based on the orientation of the glutamate moiety, and subsequently ranked by predicted affinity scores (kcal/mol). The best 16 poses for each isomer were then chosen and analyzed.

Our simulations suggest that TCP_{fast} can enter as a free ligand in both conformational states and that several binding modes are possible, depending on which the NHS ester anchoring group lies in close proximity of different nucleophilic groups (Figure S25) and potentially collides with them. In particular, we identified five lysine residues (Lys20.A, Lys21.A, Lys60.A, Lys204.A, Lys258.A) and one arginine residue (Arg172.A) as putative sites for conjugation, all located at the entrance of the binding pocket. Notably, we determined by sequence alignment that Arg172.A in GluA2 corresponds to Lys734 in GluK1, previously identified as the main site for conjugation of TCP9 and TCP10 in our first work on tethered covalent photoswitches of endogenous kainate receptors[10].

Interestingly, analysis of the binding energies predicted for the best 16 poses obtained in our docking simulations (Figure S26) revealed that *cis*-TCP_{fast} should have higher affinity for GluA2 than the *trans* isomer when the anchoring tail lies in proximity of the receptor surface, which was expected since there is not a straight pathway for the glutamate moiety from the putative conjugation sites to the binding pocket, and thus the “bent” *cis*-TCP_{fast} isomer should lead to better

binding and receptor activation. Our results *in silico* agree and partially account for the photodependent effects observed *in vitro* and *in vivo* after conjugation of our covalent photoswitch.

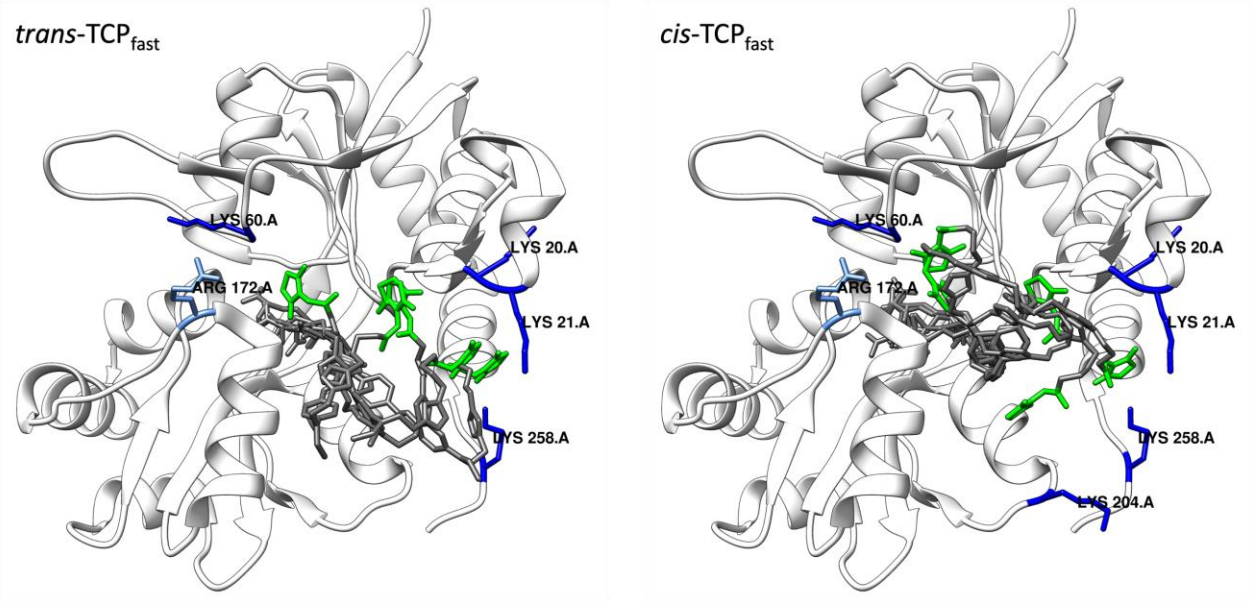

Figure S25. Representative binding modes (gray molecules) of *trans* (left panel) and *cis* (right panel) TCP$_{fast}$ in the crystal structure of the agonist binding domain of GluA2 (PDB 5FHM). The figure shows the potential conjugation sites of TCP$_{fast}$ based on the proximity between the anchoring NHS ester group (in green) and the solvent exposed lysine residues (in blue) at the entrance of the glutamate binding site. The arginine residue Arg172.A, corresponding to the lysine residue Lys734 of GluK1, is also shown (in light blue).

	predicted binding energy (kcal/mol)	
pose number	***trans*-TCP$_{fast}$**	***cis*-TCP$_{fast}$**
1	-7,6	-8,2
2	-7,5	-8,2
3	-7,4	-8,0
4	-7,4	-8,0
5	-7,2	-7,9
6	-7,2	-7,9
7	-7,1	-7,9
8	-7,0	-7,7
9	-7,0	-7,7
10	-7,0	-7,6
11	-7,0	-7,6
12	-7,0	-7,6
13	-6,9	-7,5
14	-6,9	-7,5
15	-6,8	-7,5
16	-6,7	-7,4
average ± S.D.	**-7,1 ± 0,3**	**-7,8 ± 0,3**

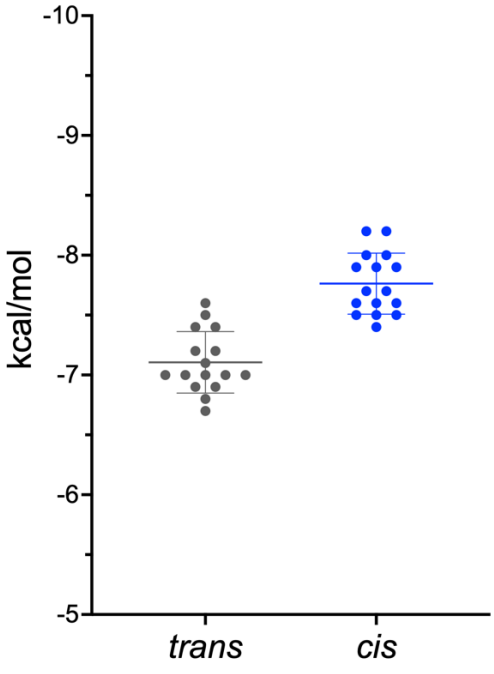

Figure S26. Predicted binding energies (kcal/mol) and graphical analysis for *trans* and *cis* TCP$_{fast}$ (best 16 poses) docked in the crystal structure of the GluA2 agonist binding domain (PDB 5FHM).

9. Supporting references

(1) Volgraf, M.; Gorostiza, P.; Numano, R.; Kramer, R. H.; Isacoff, E. Y.; Trauner, D. Allosteric Control of an Ionotropic Glutamate Receptor with an Optical Switch. *Nat. Chem. Biol.* **2006**, *2* (1), 47–52. https://doi.org/10.1038/nchembio756.

(2) Himo, F.; Lovell, T.; Hilgraf, R.; Rostovtsev, V. V.; Noodleman, L.; Sharpless, K. B.; Fokin, V. V. Copper(I)-Catalyzed Synthesis of Azoles. DFT Study Predicts Unprecedented Reactivity and Intermediates. *J. Am. Chem. Soc.* **2005**, *127* (1), 210–216. https://doi.org/10.1021/ja0471525.

(3) Russell, I. J. Origin of the Receptor Potential in Inner Hair Cells of the Mammalian Cochlea--Evidence for Davis' Theory. *Nature* **1983**, *301* (5898), 334–336.

(4) Dallos, P.; Schoeny, Z. G.; Cheatham, M. A. Cochlear Summating Potentials. Descriptive Aspects. *Acta Oto-Laryngol. Suppl.* **1972**, *302*, 1–46.

(5) Pujol, R.; Lenoir, M.; Robertson, D.; Eybalin, M.; Johnstone, B. M. Kainic Acid Selectively Alters Auditory Dendrites Connected with Cochlear Inner Hair Cells. *Hear. Res.* **1985**, *18* (2), 145–151. https://doi.org/10.1016/0378-5955(85)90006-1.

(6) Kujawa, S. G.; Liberman, M. C. Adding Insult to Injury: Cochlear Nerve Degeneration after "Temporary" Noise-Induced Hearing Loss. *J. Neurosci.* **2009**, *29* (45), 14077–14085. https://doi.org/10.1523/JNEUROSCI.2845-09.2009.

(7) Liberman, L. D.; Suzuki, J.; Liberman, M. C. Dynamics of Cochlear Synaptopathy after Acoustic Overexposure. *J. Assoc. Res. Otolaryngol. JARO* **2015**, *16* (2), 205–219. https://doi.org/10.1007/s10162-015-0510-3.

(8) Meyer, A. C.; Frank, T.; Khimich, D.; Hoch, G.; Riedel, D.; Chapochnikov, N. M.; Yarin, Y. M.; Harke, B.; Hell, S. W.; Egner, A.; Moser, T. Tuning of Synapse Number, Structure and Function in the Cochlea. *Nat. Neurosci.* **2009**, *12* (4), 444–453. https://doi.org/10.1038/nn.2293.

(9) Bourien, J.; Tang, Y.; Batrel, C.; Huet, A.; Lenoir, M.; Ladrech, S.; Desmadryl, G.; Nouvian, R.; Puel, J.-L.; Wang, J. Contribution of Auditory Nerve Fibers to Compound Action Potential of the Auditory Nerve. *J. Neurophysiol.* **2014**, *112* (5), 1025–1039. https://doi.org/10.1152/jn.00738.2013.

(10) Izquierdo-Serra, M.; Bautista-Barrufet, A.; Trapero, A.; Garrido-Charles, A.; Díaz-Tahoces, A.; Camarero, N.; Pittolo, S.; Valbuena, S.; Pérez-Jiménez, A.; Gay, M.; García-Moll, A.; Rodríguez-Escrich, C.; Lerma, J.; de la Villa, P.; Fernández, E.; Pericàs, M. À.; Llebaria, A.; Gorostiza, P. Optical Control of Endogenous Receptors and Cellular Excitability Using Targeted Covalent Photoswitches. *Nat. Commun.* **2016**, *7*, 12221. https://doi.org/10.1038/ncomms12221.

(11) Waterhouse, A. M.; Procter, J. B.; Martin, D. M. A.; Clamp, M.; Barton, G. J. Jalview Version 2--a Multiple Sequence Alignment Editor and Analysis Workbench. *Bioinforma. Oxf. Engl.* **2009**, *25* (9), 1189–1191. https://doi.org/10.1093/bioinformatics/btp033.

(12) Trott, O.; Olson, A. J. AutoDock Vina: Improving the Speed and Accuracy of Docking with a New Scoring Function, Efficient Optimization, and Multithreading. *J. Comput. Chem.* **2010**, *31* (2), 455–461. https://doi.org/10.1002/jcc.21334.

(13) Pettersen, E. F.; Goddard, T. D.; Huang, C. C.; Couch, G. S.; Greenblatt, D. M.; Meng, E. C.; Ferrin, T. E. UCSF Chimera--a Visualization System for Exploratory Research and Analysis. *J. Comput. Chem.* **2004**, *25* (13), 1605–1612. https://doi.org/10.1002/jcc.20084.

(14) Wang, S.-Y.; Larsen, Y.; Navarrete, C. V.; Jensen, A. A.; Nielsen, B.; Al-Musaed, A.; Frydenvang, K.; Kastrup, J. S.; Pickering, D. S.; Clausen, R. P. Tweaking Subtype Selectivity and Agonist Efficacy at (S)-2-Amino-3-(3-Hydroxy-5-Methyl-Isoxazol-4-Yl)Propionic Acid

(AMPA) Receptors in a Small Series of BnTetAMPA Analogues. *J. Med. Chem.* **2016**, *59* (5), 2244–2254. https://doi.org/10.1021/acs.jmedchem.5b01982.

(15) Shrestha, B. R.; Chia, C.; Wu, L.; Kujawa, S. G.; Liberman, M. C.; Goodrich, L. V. Sensory Neuron Diversity in the Inner Ear Is Shaped by Activity. *Cell* **2018**, *174* (5), 1229-1246.e17. https://doi.org/10.1016/j.cell.2018.07.007.